AGU ADVANCING EARTH AND SPACE SCIENCE

JGR Solid Earth

RESEARCH ARTICLE

10.1029/2020JB021175

Resolving Wave Propagation in Anisotropic Poroelastic Media Using Graphical Processing Units (GPUs)

Yury Alkhimenkov[1,2,3], **Ludovic Räss**[4,5], **Lyudmila Khakimova**[3,6], **Beatriz Quintal**[1,2], and **Yury Podladchikov**[1,2,3]

[1]Institute of Earth Sciences, University of Lausanne, Lausanne, Switzerland, [2]Swiss Geocomputing Centre, University of Lausanne, Lausanne, Switzerland, [3]Faculty of Mechanics and Mathematics, Lomonosov Moscow State University, Moscow, Russia, [4]Laboratory of Hydraulics, Hydrology and Glaciology (VAW), ETH Zurich, Zurich, Switzerland, [5]Swiss Federal Institute for Forest, Snow and Landscape Research (WSL), Birmensdorf, Switzerland, [6]Skoltech Center for Hydrocarbon Recovery, Skolkovo Institute of Science and Technology, Moscow, Russia

Key Points:

- We present the dimensional analysis of Biot's equations
- We perform three dimensional numerical simulations of poroelastic wave propagation
- We propose a multi-graphical processing units implementation resolving over 1.5 billion grid cells in a few seconds with near ideal parallel efficiency

Correspondence to:

Y. Alkhimenkov,
yury.alkhimenkov@unil.ch

Citation:

Alkhimenkov, Y., Räss, L., Khakimova, L., Quintal, B., & Podladchikov, Y. (2021). Resolving wave propagation in anisotropic poroelastic media using graphical processing units (GPUs). *Journal of Geophysical Research: Solid Earth*, *126*, e2020JB021175. https://doi.org/10.1029/2020JB021175

Received 16 OCT 2020
Accepted 28 FEB 2021

Author Contributions:

Conceptualization: Yury Alkhimenkov, Beatriz Quintal, Yury Podladchikov
Formal analysis: Yury Alkhimenkov
Investigation: Yury Alkhimenkov
Methodology: Yury Alkhimenkov, Ludovic Räss, Lyudmila Khakimova, Beatriz Quintal, Yury Podladchikov
Project Administration: Yury Alkhimenkov
Software: Yury Alkhimenkov, Ludovic Räss, Lyudmila Khakimova, Yury Podladchikov
Supervision: Beatriz Quintal, Yury Podladchikov
Visualization: Yury Alkhimenkov, Ludovic Räss, Lyudmila Khakimova
Writing – original draft: Yury Alkhimenkov

Abstract Biot's equations describe the physics of hydromechanically coupled systems establishing the widely recognized theory of poroelasticity. This theory has a broad range of applications in Earth and biological sciences as well as in engineering. The numerical solution of Biot's equations is challenging because wave propagation and fluid pressure diffusion processes occur simultaneously but feature very different characteristic time scales. Analogous to geophysical data acquisition, high resolution and three dimensional numerical experiments lately redefined state of the art. Tackling high spatial and temporal resolution requires a high-performance computing approach. We developed a multi- graphical processing units (GPU) numerical application to resolve the anisotropic elastodynamic Biot's equations that relies on a conservative numerical scheme to simulate, in a few seconds, wave fields for spatial domains involving more than 1.5 billion grid cells. We present a comprehensive dimensional analysis reducing the number of material parameters needed for the numerical experiments from ten to four. Furthermore, the dimensional analysis emphasizes the key material parameters governing the physics of wave propagation in poroelastic media. We perform a dispersion analysis as function of dimensionless parameters leading to simple and transparent dispersion relations. We then benchmark our numerical solution against an analytical plane wave solution. Finally, we present several numerical modeling experiments, including a three-dimensional simulation of fluid injection into a poroelastic medium. We provide the Matlab, symbolic Maple, and GPU CUDA C routines to reproduce the main presented results. The high efficiency of our numerical implementation makes it readily usable to investigate three-dimensional and high-resolution scenarios of practical applications.

1. Introduction

Majority of the most powerful supercomputers on the world host hardware accelerators to sustain calculations at the petascale level and beyond. Graphical processing units (GPUs) are amongst widely employed hardware accelerators, initiating a revolution in high-performance computing (HPC) in the last decade. The three-dimensional calculations targeting billions of grid cells – technically impossible resolutions decades ago – became reality. This major breakthrough in HPC and supercomputing comes however with the cost of developing and reengineering scientific codes to efficiently utilize the available computing power. Increasing the low-level parallelism is the key. In Earth sciences, HPC and GPU-accelerated applications target in particular forward and inverse seismic modeling and geodynamics – fields where high spatial and temporal resolutions as well as large spatial domains are required. We here develop a multi-GPU implementation for applications in seismic modeling in porous media.

Understanding seismic wave propagation in fluid-saturated porous media enables more accurate interpretation of seismic signals in Earth sciences. The two phase medium is represented by an elastic solid matrix (skeleton) saturated with a compressible viscous fluid. The dynamic response of such an isotropic two phase medium results in two longitudinal waves and one shear wave, as predicted by Frenkel (1944) (see also Pride and Garambois (2005)). The wave of the first kind (fast wave) is a true longitudinal wave where the solid matrix motion and the fluid velocity vector fields are in-phase. The wave of the second kind (slow wave) is a highly attenuated wave where the solid matrix motion and the fluid velocity vector fields are

Writing – review & editing: Ludovic Räss, Lyudmila Khakimova, Beatriz Quintal, Yury Podladchikov

out-of-phase. Depending on the medium's properties, the slow wave may propagate as a longitudinal wave, or it may diffuse and attenuate quickly. Maurice Anthony Biot performed systematic studies of solid-fluid deformation in porous media based on the Hamiltonian principle of least action. He first investigated a static loading known as the theory of consolidation (Biot, 1941; Biot & Willis, 1957). The mathematical description of the macroscopic coupled solid-fluid deformation in a porous medium is analogous to the theory of thermoelasticity (Biot, 1941; Zimmerman, 2000). Biot later developed the theory of poroelasticity or Biot's theory for wave propagation in fluid-saturated media (Biot, 1956a, 1956b). Biot summarized these results in Biot (1962a); Biot (1962b) and provided a final set of unknown fields, parameters, as well as, a guidance to expand poroelasticity to include viscoelasticity and non-linear effects (Biot, 1965). Fluid flow in porous media in Biot's theory is assumed to be laminar, described by Darcy's law (Biot, 1956b), and is usually referred to as the low frequency Biot's theory. If the fluid flow is accelerated, viscous boundary layers form in the pores and a slight modification of Biot's equations is needed to account for this high frequency effect (Biot, 1956a). We focus in this study on the low frequency Biot's theory (Biot, 1956b). A detailed analysis of the coupled solid-fluid deformation in a porous media can be found in various recent studies, for example Bourbié et al. (1987); Wang (2000); Cheng (2016). Approximations based on this theory are widely used in biology and medical imaging, and in Earth sciences (e.g., Carcione (2014)), they are used in seismic exploration, seismic monitoring of geological CO_2 sequestration and nuclear waste disposal, geothermal energy production and hydrogeology.

One of the main application of Biot's equations in Earth sciences is the estimation of seismic dispersion and attenuation in porous media due to wave-induced fluid flow. Several wave attenuation mechanisms related to fluid flow arise from Biot's theory (Müller et al., 2010; Pride et al., 2004). The first attenuation mechanism introduced by Biot is the global fluid flow, which occurs at the wavelength scale of a propagating wave. In this mechanism, the dissipation is caused by the relative fluid motion between the solid matrix and the fluid (Biot, 1956b). The second mechanism is the wave-induced fluid flow at the mesoscopic scale. This scale is defined as much larger than the sizes of individual pores but much smaller than the wavelength of a propagating wave (Pride et al., 2004; White et al., 1975). In this mechanism, the dissipation is caused due to fluid-pressure gradients arising between mesoscopic heterogeneities in the medium. For example, fluid-pressure gradients appear between highly permeable structures such as fractures and the embedding solid matrix of much lower permeability. Wave-induced fluid flow at microscopic scale also occurs and is referred to as squirt flow, in which fluid-pressure gradients take place between compliant and stiff pores (Dvorkin et al., 1995; Mavko & Nur, 1975). Other mechanisms involve different kinds of wave scattering and wave mode conversions at interfaces. Possible non-linear viscous and plastic effects are small for most of the applications in applied seismic and are then neglected under the linear approximation assumption.

The aforementioned analytical approaches for wave-induced fluid flow at global and mesoscopic scales mainly exist for simple geometries. For more complex geometries, a numerical approach is needed to estimate seismic dispersion and attenuation. In principle, it can be done numerically in two ways. One approach relies on direct modeling of wave propagation in porous media and estimation of dispersion and attenuation of a propagating wavelets (Caspari et al., 2019; Masson et al., 2006). The other approach is based on a quasi-static numerical modeling and estimation of effective frequency-dependent elastic properties. The modeled frequency-dependent properties are used to retrieve dispersion and attenuation of seismic waves (Hunziker et al., 2018; Masson & Pride, 2007; Quintal et al., 2011; Rubino et al., 2009).

During the last three decades a significant number of studies targeted numerical simulations of wave propagation in poroelastic media. A detailed review of early studies is given in Carcione et al. (2010). Different methods have been used, based on combined finite-volumes/differences on structured grids (Blanc et al., 2013; Carcione & Quiroga-Goode, 1995; Chiavassa et al., 2010; Chiavassa & Lombard, 2011; Dai et al., 1995; Masson et al., 2006; Özdenvar & McMechan, 1997; Wenzlau & Müller, 2009; Zeng et al., 2001; Zhu & McMechan, 1991), pseudo-spectral methods (Özdenvar & McMechan, 1997), discontinuous Galerkin methods (de la Puente et al., 2008; Dupuy et al., 2011; Shukla et al., 2019, 2020; Ward et al., 2017; Zhan et al., 2019), spectral element methods (Morency & Tromp, 2008), and finite-volume methods (Lemoine, 2016; Lemoine et al., 2013). Most of these studies implemented the corresponding equations as a first-order hyperbolic system and used explicit time integration schemes as it is convenient for the elastic wave propagation, except for (Morency & Tromp, 2008; Özdenvar & McMechan, 1997), where a

second-order system was considered. Moczo et al. (2019) and Gregor et al. (2021) investigated the accuracy of the discrete characterization of material heterogeneities and subcell-resolution for the finite-difference modeling of Biot's equations.

A major challenge in the numerical modeling of Biot's equations relies in the treatment of the dissipation term in the equations of motions. This term is represented by a parabolic operator coupled to viscosity, permeability, and density and, affects the numerical stability of the entire system of equations. The diffusion process exhibits a much larger characteristic time scale then the wave propagation process, which makes Biot's equations "stiff," thus challenging to solve. A straightforward explicit time integration of a "stiff" system is possible but requires very small time steps and is computationally inefficient. Various studies discuss stability conditions in the scope of poroelastic wave propagation and report a series of issues (Carcione & Quiroga-Goode, 1995; Chiavassa & Lombard, 2011; Masson et al., 2006). A more detailed discussion regarding the stability of discrete schemes of Biot's equations can be found in Alkhimenkov et al. (2020).

We here propose a multi-GPU numerical implementation of the anisotropic elastodynamic Biot's equations building upon three key ideas: Concise numerical implementation, high numerical resolution, and high computational efficiency. A concise numerical implementation means that we designed a simple and short numerical code ensuring it is suitable for parallel GPU devices. We use a variant of a conservative staggered space-time grid discretization (Virieux, 1986), which is equivalent to a finite volume approach (Dormy & Tarantola, 1995). High numerical spatial resolution up to six billion grid cells permits us to resolve very complex geometries. High computational efficiency allows our numerical model to simulate, in a few seconds only, wave fields in domains involving over 1.5 billion grid cells. We further explore several aspects of Biot's equations, namely, wave propagation in poroelastic isotropic and anisotropic media, fluid diffusion, dimensional and dispersion analyses, and numerical stability. The resulting code is implemented in CUDA C, which is suitable for programmable Nvidia GPU devices. The choice of a rectangular grid is determined by the usage of GPUs, so that the numerical implementation is straightforward. We provide the Matlab, symbolic Maple, and GPU CUDA C routines to reproduce the main presented results. These routines are available for download from Bitbucket at https://bitbucket.org/yalkhimenkov/fastbiot_gpu3d_v1.0 (last access: February 8, 2021). The routines archive (v1.0) (Alkhimenkov et al., 2021) is available from a permanent DOI repository (Zenodo) at http://doi.org/10.5281/zenodo.4519367 (last access: February 8, 2021).

The novelties of the present article are summarized as following:

1. We present a dimensional analysis, reducing the number of needed material parameters from ten to four.
2. We perform a dispersion analysis as a function of dimensionless parameters.
3. We achieve a close-to-ideal parallel efficiency (98% and 96%) on a weak scaling tests up to 128 GPUs and an effective memory throughput efficiency of 90% for the 3D anisotropic poroelastic wave propagation code.
4. We achieve a very fast execution time (seconds) using high-resolution models involving more than 1.5 billion grid cells.

2. Elastodynamic Biot's Equations in Isotropic Media

2.1. Constitutive Equations

We describe the elastodynamic Biot's equations for an isotropic medium saturated with a single phase fluid. We use a classical velocity-stress formulation for the Biot's equations. The equations describing a two phase continuum mainly differ from the single phase continuum formulation (see Appendix A) by the presence of both solid and fluid velocities and, as well as both solid and fluid pressure fields. Furthermore, the scalar parameters linking stresses and velocities in the single phase continuum become a symmetric coefficient matrix in the two phase continuum. The set of equations describing a two phase continuum (solid and fluid) was formulated in the theory of poroelasticity (Biot, 1956b, 1962a). The symmetric coefficient matrix is positive definite, which directly follows from the elastic potential energy. Biot's equations can be written in a symmetric form by separating volumetric and deviatoric parts of the stress tensor. Lists of symbols are given in Tables 1 and 2. The constitutive equations are (Biot, 1962a; Pride et al., 2004; Wang, 2000; Yarushina & Podladchikov, 2015)

Table 1
List of Principal Notation

Symbol	Meaning	Unit
σ^s, σ^f	solid and fluid stress	Pa
p_s, p_f	solid and fluid pressure	Pa
τ^s, τ^f	solid and fluid stress deviator	Pa
v^s, v^f	solid and fluid velocity	m/s
ρ^s, ρ^f	solid and fluid density	kg/m^3
K_g, K_f	elastic solid and fluid bulk modulus	Pa
G_g, G	elastic solid and drained shear modulus	Pa
K_d, K_u	elastic drained and undrained bulk modulus	Pa
η	fluid shear viscosity	Pa·s
k	Permeability	m^2
ϕ	Porosity	-

$$\begin{pmatrix} \nabla_k v_k^s \\ \nabla_k q_k^D \end{pmatrix} = -\frac{1}{K_d}\begin{pmatrix} 1 & -\alpha \\ -\alpha & \frac{\alpha}{B} \end{pmatrix}\begin{pmatrix} \frac{\partial \overline{p}}{\partial t} \\ \frac{\partial p_f}{\partial t} \end{pmatrix} \tag{1}$$

and

$$\frac{\partial \overline{\tau}_{ij}}{\partial t} = 2G\left(\frac{1}{2}(\nabla_j v_i^s + \nabla_i v_j^s) - \frac{1}{3}(\nabla_k v_k^s)\delta_{ij}\right), \tag{2}$$

linking the stress-strain relations for the solid and fluid phases with the conservation of mass (Equation 1) and representing the deviatoric stress-strain relation for the solid phase (Equation 2). The constitutive Equations 1 and 2 are written for the total pressure $\overline{p}$ and fluid pressure p_f, as it was originally suggested in Biot (1962a). The porosity ϕ in Darcy's flux q_i^D is constant in time but can be different spatially throughout the model domain.

For an isotropic material saturated with a single fluid, in which the solid frame consists of a single isotropic mineral, the Biot-Willis coefficient is

$$\alpha = 1 - K_d / K_g = \left(1 - K_d / K_u\right) / B, \tag{3}$$

where K_u is the undrained bulk modulus

$$K_u = K_d + \alpha^2 M, \tag{4}$$

M is the fluid storage coefficient

$$M = \left(\phi / K_f + (1-\phi) / K_g - K_d / K_g^2\right)^{-1} \tag{5}$$

or

$$M = BK_u / \alpha, \tag{6}$$

and the Skempton's coefficient B reads

$$B = \frac{1 / K_d - 1 / K_g}{1 / K_d - 1 / K_g + \phi(1 / K_f - 1 / K_g)}. \tag{7}$$

Table 2
Shorthand Notations

Symbol	Meaning
$\overline{p}$	$= \left(1-\phi\right)p_s + \phi p_f$, total pressure
$\overline{\sigma}$	total stress
$\overline{\tau}$	total stress deviator
q_i^D	$= \phi(v_i^f - v_i^s)$, Darcy's flux
ρ_t	$= \left(1-\phi\right)\rho_s + \phi\rho_f$, total density
α	Biot-Willis coefficient
B	Skempton's coefficient
δ_{ij}	Kronecker delta

2.2. Dynamic Equations

The conservation of linear momentum (Newton's second law or dynamic equations) can be written in a symmetric form (Biot, 1962a; Pride et al., 2004; Wang, 2000; Yarushina & Podladchikov, 2015)

$$\begin{pmatrix} \nabla_j\left(-\overline{p}\delta_{ij} + \overline{\tau}_{ij}\right) \\ \frac{\eta}{k} q_i^D + \nabla_i p_f \end{pmatrix} = \begin{pmatrix} \rho_t & -\rho_f \\ -\rho_f & \rho_a \end{pmatrix}\begin{pmatrix} \frac{\partial v_i^s}{\partial t} \\ -\frac{\partial q_i^D}{\partial t} \end{pmatrix}, \tag{8}$$

where $\rho_a = \rho_f T / \phi$, T is the tortuosity and $i, j, k = \overline{1,\ldots,3}$. The off-diagonal parameter fluid density ρ_f can be considered as the added mass

coefficient. Equation 8 is analogous to that of a single phase media (Equation (A11)), the only difference being the substitution of the scalar density by a coefficient matrix with same dimensions.

Equations 1–8 are the elastodynamic Biot's equations for an isotropic medium saturated with a single phase fluid. The experiments to obtain poroelastic parameters are given in Appendix B. We emphasize that the matrices of coefficients in Equations 1 and 8 are symmetric. This symmetry combined with the non-dimensional analysis make it possible to derive the dispersion relations in a simple explicit form using symbolic calculations (Maple).

3. Dimensional Analysis of the Elastodynamic Biot's Equations

Dimensional analysis of PDEs unveils the impact of various physical parameters on the considered physical system. The original Biot's Equations 1–8 contain many material parameters making it difficult to understand how they affect the response of a poroelastic continuum. For enhanced clarity, we present a dimensional analysis of the elastodynamic Biot's equations. This analysis reduces the number of material parameters from ten to four, isolating the governing independent physical quantities.

For conciseness, we present our physical system as a one dimensional example to express the total stress tensor as a combination of the volumetric and deviatoric stresses (the entire analysis can be applied to three-dimensional continuum)

$$\frac{\partial \bar{\sigma}}{\partial t} = -\frac{\partial \bar{p}}{\partial t} + \frac{\partial \bar{\tau}}{\partial t} \tag{9}$$

we introduce the compliance $s_{11}^d \left[\mathrm{Pa}^{-1}\right]$ and the total density $\rho_t \left[\mathrm{kg/m}^3\right]$ to express Equations 1, 2, and 8 in a dimensionless form. Compliance s_{11}^d relates to the drained bulk modulus K_d and the shear modulus G

$$s_{11}^d = 1 / (K_d + 4 / 3G), \tag{10}$$

which has dimensions of $\left[\mathrm{Pa}^{-1}\right]$. We first extract s_{11}^d and ρ_t out of the parentheses in Equations 1, 2, and 8 (leaving only dimensionless parameters inside). We reformulate the system using Equation 9 as

$$s_{11}^d \begin{pmatrix} 1 & -\alpha \\ -\alpha & \alpha_a \end{pmatrix} \begin{pmatrix} -\dfrac{\partial \bar{\sigma}}{\partial t} \\ \dfrac{\partial p_f}{\partial t} \end{pmatrix} = -\begin{pmatrix} \dfrac{\partial v^s}{\partial x} \\ \dfrac{\partial q^D}{\partial x} \end{pmatrix} \tag{11}$$

and

$$\rho_t \begin{pmatrix} 1 & -\dfrac{\rho_f}{\rho_t} \\ -\dfrac{\rho_f}{\rho_t} & \dfrac{\rho_a}{\rho_t} \end{pmatrix} \begin{pmatrix} \dfrac{\partial v^s}{\partial t} \\ -\dfrac{\partial q^D}{\partial t} \end{pmatrix} = \begin{pmatrix} \dfrac{\partial \bar{\sigma}}{\partial x} \\ \dfrac{\eta}{k} q^D + \dfrac{\partial p_f}{\partial x} \end{pmatrix}, \tag{12}$$

where

$$\alpha_a = \frac{\alpha}{B}\left(1 + \frac{4 / 3G}{K_u}\right), \tag{13}$$

is a dimensionless parameter (the apparent Biot-Willis coefficient).

We then substitute

$$\bar{\sigma} \rightarrow \frac{1}{s_{11}^d}\tilde{\bar{\sigma}}, p_f \rightarrow \frac{1}{s_{11}^d}\tilde{p}_f, \tag{14}$$

$$v^s \rightarrow \frac{L_x^*}{\tau^*}\tilde{v}^s, q^D \rightarrow \frac{L_x^*}{\tau^*}\tilde{q}^D, \tag{15}$$

$$x \rightarrow L_x^*\tilde{x}, t \rightarrow \tau^*\tilde{t}, \tag{16}$$

where $L_x^*\left[\mathrm{m}\right]$ is the characteristic length, $\tau^*\left[\mathrm{s}\right]$ is the characteristic time and the superscript ~ refers to the dimensionless quantities. The resulting system of equations reads

$$\begin{pmatrix} 1 & -\alpha \\ -\alpha & \alpha_a \end{pmatrix} \begin{pmatrix} -\dfrac{\partial\tilde{\bar{\sigma}}}{\partial\tilde{t}} \\ \dfrac{\partial\tilde{p}_f}{\partial\tilde{t}} \end{pmatrix} = -\begin{pmatrix} \dfrac{\partial\tilde{v}^s}{\partial\tilde{x}} \\ \dfrac{\partial\tilde{q}^D}{\partial\tilde{x}} \end{pmatrix} \tag{17}$$

and

$$\left(I_1\right)^2 \begin{pmatrix} 1 & -\rho_{ft} \\ -\rho_{ft} & \rho_{at} \end{pmatrix} \begin{pmatrix} \dfrac{\partial\tilde{v}^s}{\partial\tilde{t}} \\ -\dfrac{\partial\tilde{q}^D}{\partial\tilde{t}} \end{pmatrix} = \begin{pmatrix} \dfrac{\partial\tilde{\bar{\sigma}}}{\partial\tilde{x}} \\ I_2\tilde{q}^D + \dfrac{\partial\tilde{p}_f}{\partial\tilde{x}} \end{pmatrix}, \tag{18}$$

where $\rho_{ft} \equiv \rho_f/\rho_t$, $\rho_{at} \equiv \rho_a/\rho_t$,

$$I_1 = \sqrt{\rho_t s_{11}^d}\frac{L_x^*}{\tau^*} \equiv \frac{1}{V_d}\frac{L_x^*}{\tau^*}, \tag{19}$$

$$V_d = \sqrt{\frac{1}{\rho_t s_{11}^d}} \tag{20}$$

and

$$I_2 = \frac{\eta s_{11}^d}{k}\frac{(L_x^*)^2}{\tau^*} \equiv \frac{1}{D}\frac{(L_x^*)^2}{\tau^*}, \tag{21}$$

$$D = \frac{k}{\eta s_{11}^d}. \tag{22}$$

The four dimensionless parameters α, α_a, ρ_{ft}, and ρ_{at} define the coupling between the solid and fluid phase. The two key dimensionless parameters I_1 and I_2 denote the ratio between advection and diffusion time scales and relate to hyperbolic (advection) and parabolic (diffusion) processes, respectively. The pore fluid pressure transport time scale

$$\tau_d^* = \frac{(L_x^*)^2}{D} \tag{23}$$

refers to the characteristic time scale of diffusive processes. The elastic travel time scale

$$\tau_a^* = \frac{L_x^*}{V_d} \tag{24}$$

refers to the characteristic time scale of advection processes. In order to further reduce the number of parameters, we set $I_1 = 1$. From Equation 19, $L_x^* = \tau^* V_d$, therefore, Equation 21 becomes

$$I_2 = \frac{\eta}{k\rho_t}\tau^*, \tag{25}$$

where τ^* is a free parameter. We further choose τ^* as

$$\tau^* = \left(\frac{\eta}{k\rho_t}\right)^{-1}. \tag{26}$$

Equation 25 becomes

$$I_2 = \frac{\eta}{k\rho_t}\tau^* = \frac{\eta}{k\rho_t}\left(\frac{\eta}{k\rho_t}\right)^{-1} \equiv 1 \tag{27}$$

Taking into account that $I_1 = 1$ and $I_2 = 1$, we reformulate Equation 18 as

$$\begin{pmatrix} 1 & -\rho_{ft} \\ -\rho_{ft} & \rho_{at} \end{pmatrix} \begin{pmatrix} \frac{\partial \tilde{v}^s}{\partial \tilde{t}} \\ -\frac{\partial \tilde{q}^D}{\partial \tilde{t}} \end{pmatrix} = \begin{pmatrix} \frac{\partial \tilde{\bar{\sigma}}}{\partial \tilde{x}} \\ \tilde{q}^D + \frac{\partial \tilde{p}_f}{\partial \tilde{x}} \end{pmatrix}. \tag{28}$$

Equations 17 and 28 are the dimensionless elastodynamic Biot's equations for an isotropic medium saturated with a single fluid featuring only four dimensionless parameters: α, α_a, ρ_{ft}, and ρ_{at}.

3.1. Dispersion Analysis of the Elastodynamic Biot's Equations

We perform dispersion analysis to understand the behavior of the dimensionless elastodynamic Biot's Equations 17 and 18. For simplicity, we only consider longitudinal waves. A single harmonic plane wave solution is

$$W = Ae^{-i(\omega t - kl)}, \tag{29}$$

where A is the amplitude, i is the imaginary unit, $\omega = 2\pi f$ is the real angular frequency (f is the frequency), k is the complex wave number, and l is the propagation direction. This solution is substituted into the system (17)–(18), which gives

$$\begin{bmatrix} i\omega & i\omega\alpha & ik & 0 \\ -i\omega\alpha & -i\omega\alpha_a & 0 & ik \\ -ik & 0 & -i\omega(I_1)^2 & -i\omega(I_1)^2\rho_{ft} \\ 0 & -ik & i\omega(I_1)^2\rho_{ft} & i\omega(I_1)^2\rho_{at} - I_2 \end{bmatrix} \tag{30}$$

The dispersion relation for longitudinal waves is

$$k^4 - a_2k^2 + a_0 = 0, \tag{31}$$

where

$$a_2 = \left(1 + \rho_{at}\alpha_a - 2\rho_{ft}\alpha\right)(I_1)^2\omega^2 + i\omega\alpha_a I_2 \tag{32}$$

$$a_0 = (I_1)^4\left(\rho_{ft}^2 - \rho_{at}\right)\left(\alpha^2 - \alpha_a\right)\omega^4 - i\omega^3\left(\alpha^2 - \alpha_a\right)(I_1)^2 I_2 \tag{33}$$

Equation 31 is bi-quadratic with respect to k, the four roots ($\pm k_1$ and $\pm k_2$) are the complex functions of the non-dimensional angular frequency ω

$$k_{1,2} = \pm\sqrt{\frac{a_2 \mp \sqrt{a_2^2 - 4a_0}}{2}} \tag{34}$$

The non-dimensional fast and slow wave phase velocities are

$$\tilde{V}_1 = \omega / \mathrm{Re}(k_1), \tilde{V}_2 = \omega / \mathrm{Re}(k_2) \tag{35}$$

The inverse quality factors are defined as

$$\frac{1}{Q_1} = \frac{\mathrm{Im}(k_1^2)}{\mathrm{Re}(k_1^2)}, \frac{1}{Q_2} = \frac{\mathrm{Im}(k_2^2)}{\mathrm{Re}(k_2^2)}. \tag{36}$$

If $I_2 \equiv 0$, the fast and slow waves become the real and non-dispersive functions of the angular frequency ω. Since $I_2 \equiv 0$ eliminates $\tilde{q}^D$ in 18, the system of Equations 17 and 18 becomes fully hyperbolic without the diffusive term. I_2 and the Biot-Willis coefficients α and α_a control the imaginary part of the wave numbers $\pm k_1$ and $\pm k_2$; they thus control dispersion and attenuation of the coupled system of equations. Setting $\alpha_a \equiv 0$ and $\left(\alpha^2 - \alpha_a\right) \equiv 0$ provides an alternative way to achieve real roots in 34.

Setting $I_1 = 1$ and $I_2 = 1$ and using the characteristic length ($L_x^* = \tau^* V_d$) and time ($\tau^* = \eta/(k\rho_t)$) scales permits to further simplify the dispersion relations (31)–(33) to

$$k^4 + \left(\left(2\rho_{ft}\alpha - \rho_{at}\alpha_a - 1\right)\omega^2 - i\omega\alpha_a\right)k^2 + \left(\rho_{ft}^2 - \rho_{at}\right)\left(\alpha^2 - \alpha_a\right)\omega^4 - i\omega^3\left(\alpha^2 - \alpha_a\right) = 0, \tag{37}$$

which results in a biquadratic equation with respect to k. The four roots ($\pm k_1$ and $\pm k_2$) are the complex functions of the angular frequency ω. The dispersion relation (37) is the most important result of the dimensional analysis and relates to the final set of non-dimensional elastodynamic Biot's equations (Equation 17 and 28).

Figure 1a shows the non-dimensional phase velocities and inverse quality factors based on the system of Equations 17 and 28 for a homogeneous medium, which are typical for Biot's mechanism. The properties of the medium are given in Table 3. The non-dimensional phase velocity $\tilde{V}_1$ exhibits some dispersion (less than 10%) and attenuation. The non-dimensional phase velocity $\tilde{V}_2$ behaves as a diffusion mode at low frequencies, having zero velocity. At higher frequencies, $\tilde{V}_2$ behaves as a true propagating wave. The low frequency limit of $\tilde{V}_1$ corresponds to the non-dimensional undrained phase velocity $\tilde{V}_1^{LF}$,

$$\tilde{V}_1^{LF} = \frac{1}{V_d}\sqrt{\frac{K_u + 4/3G}{\rho_t}}. \tag{38}$$

The high frequency limit of $\tilde{V}_1$ corresponds to the non-dimensional undrained phase velocity $\tilde{V}_1^{HF}$ which is larger than $\tilde{V}_1^{LF}$. We calculate $\tilde{V}_1^{HF}$ from the dispersion relations under the assumption of $\omega \to +\infty$. The explicit formula is given in the following section.

Multiplying non-dimensional phase velocities ($\tilde{V}_1$ and $\tilde{V}_2$) by the drained velocity V_d (Equation 20) permits to recover the dimensional form of the dispersion curves (Figure 1b). We retrieve the dimensional angular frequency $\omega^d = \omega\,\omega^*$, where ω is the non-dimensional angular frequency (the y-axis in Figure 1a) and ω^* is the transformation frequency

$$\omega^* = \frac{1}{\tau^*} \equiv \frac{\eta}{k\rho_t}. \tag{39}$$

We highlight that the introduced transformation frequency ω^* is similar to Biot's characteristic frequency

$$\omega_c = \frac{\eta\phi}{k\rho_f T}. \tag{40}$$

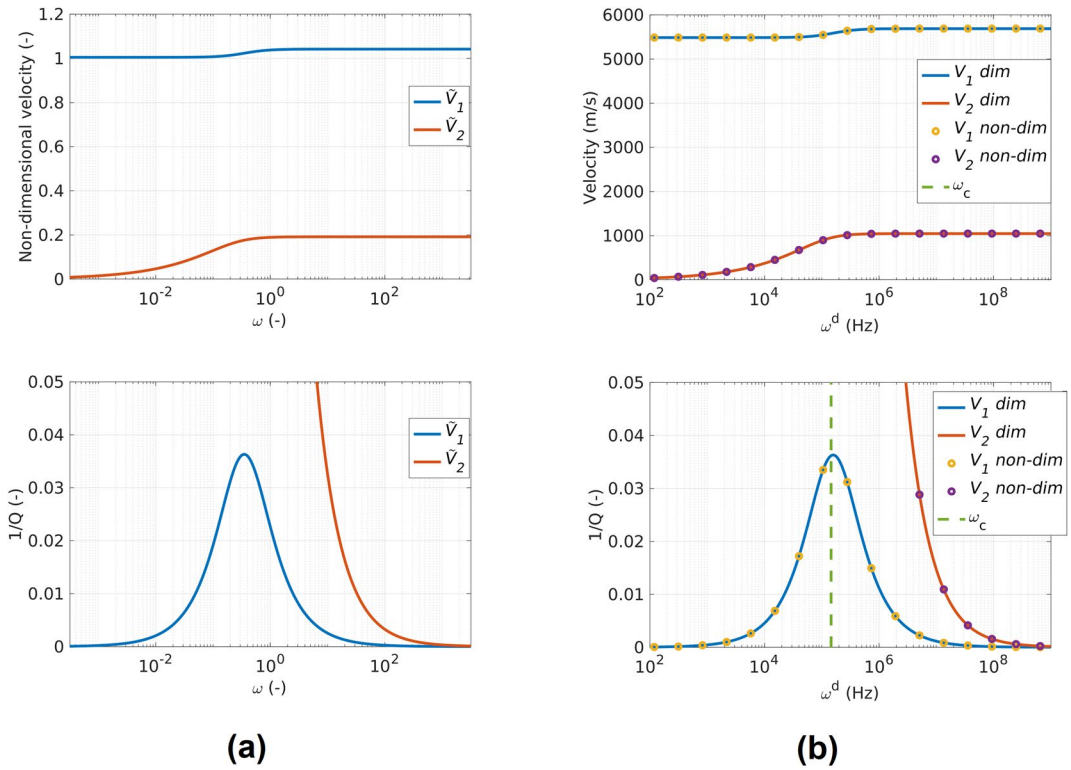

Figure 1. Phase velocities and the corresponding inverse quality factors $1/Q$ obtained via the dispersion analysis. (a) Dispersion relations for the non-dimensional elastodynamic Biot's equations, $\tilde{V}_1$ is the wave of the first kind (non-dimensional), $\tilde{V}_2$ is the wave of the second kind (non-dimensional). (b) Dispersion relations for the dimensional elastodynamic Biot's equations. V_1 dim and V_2 dim correspond to dimensional velocities, V_1 non-dim and V_2 non-dim correspond to non-dimensional velocities, which were rescaled by the dimensional characteristic velocity V_d and the transformation frequency ω^*. ω_c is the Biot's characteristic frequency. The material parameters are those from Table 3.

we detail a dimensional analysis where the transformation frequency coincides with Biot's characteristic frequency in Appendix C.

Table 3
Poroelastic Properties of Carbonate

Rock properties		Carbonate
with independent units		
K_d	(GPa)	26
$\eta_k = \eta/k$	(Pa·s/m^2)	$0.001/10^{-12} = 1 \cdot 10^9$
ρ_s	(kg/m^3)	2,700
nondimentional		
ϕ		0.3
T		1.9
with dependent units		
G	(GPa)	$15/13 \times K_d$
K_f	(GPa)	$0.0865 \times K_d$
ρ_f	(kg/m^3)	$0.4 \times \rho_s$
K_g	(GPa)	$1.42 \times K_d$

Figure 2 illustrates the advantage of the non-dimensional equations over their dimensional analog. The inverse quality factor $1/Q_1$ for the non-dimensional elastodynamic Biot's equations (Figure 2b) collapsed into the one curve considering the dimensional equations (Figure 2a).

The roots k_1 and k_2 of the dispersion relation (37) are the functions of the four material parameters and the non-dimensional angular frequency ω, that is, $k_1 = f\ (\alpha, \alpha_a, \rho_{ft}, \rho_{at})$ and $k_2 = f\ (\alpha, \alpha_a, \rho_{ft}, \rho_{at})$. Let us analyze the solutions (35) and (36) as a function of the material parameters and ω. The non-dimensional phase velocities ($\tilde{V}_1$ and $\tilde{V}_2$) and the corresponding quality factors ($1/Q_1$ and $1/Q_2$) as a function of the non-dimensional frequency ω and the Biot-Willis coefficient α are shown in Figure 3. According to (17), α controls the coupling between solid and fluid phases, low values of α (0–0.3) correspond to weak coupling and high values of α (0.7–1.0) correspond to strong coupling. We vary α in the range of (0.05, 0.95) while the other parameters remain the same. $\tilde{V}_1$ non-linearly depends on α in the whole frequency range, as α increases, $\tilde{V}_1$ also increases (Figure 3a). $1/Q_1$ linearly depends on α, as α increases, $1/Q_1$ only slightly decreases (Figure 3b). $\tilde{V}_2$ and $1/Q_2$ are almost independent of α (Figures 3c and 3d). At low frequencies, $\tilde{V}_2$ is almost zero and the quality factor $1/Q_2$ is very high (Figures 3c and 3d), which corresponds

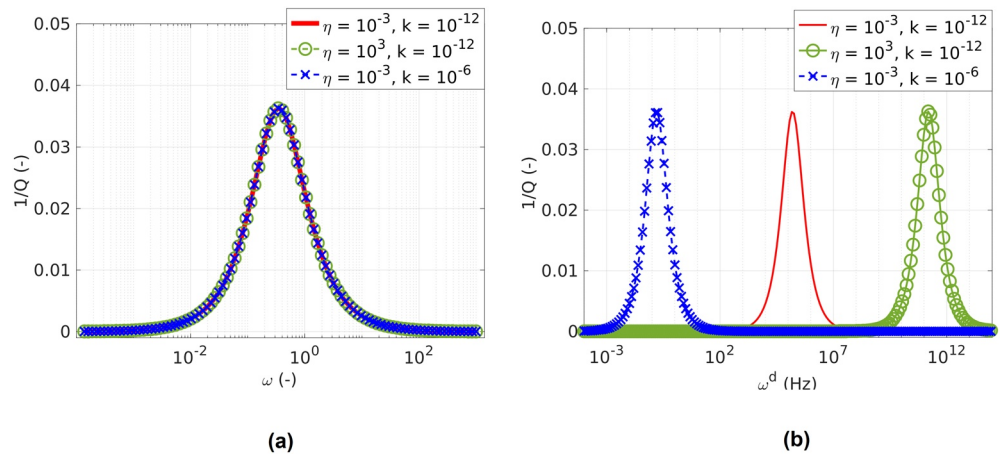

Figure 2. The inverse quality factors $1/Q$ of the the wave of the first kind. (a) $1/Q$ for the non-dimensional elastodynamic Biot's equations having different viscosities and permeabilities, all collapsed into one curve. (b) $1/Q$ for the dimensional elastodynamic Biot's equations for the same data set of viscosities and permeabilities. The material parameters are those from Table 3, except for viscosities and permeabilities.

to the diffusive regime of $\tilde{V}_2$. At high frequencies, $\tilde{V}_2$ is significant and the quality factor $1/Q_2$ is almost zero, which corresponds to the regime where the slow wave behaves as a true longitudinal wave. The characteristic frequency where the transition from the diffusive to propagation regimes occurs is not affected by α.

Figure 4 is similar to Figure 3 but instead of α, the variations of ρ_{ft} are shown. We vary ρ_{ft} in the range of $\left[0.1, \sqrt{\rho_{at}}\right]$ while the other parameters remain the same. The non-dimensional parameter ρ_{ft} controls the coupling between solid and fluid phases in the dynamic Equation 18. $\tilde{V}_1$ and $1/Q_1$ non-linearly depend on ρ_{ft}

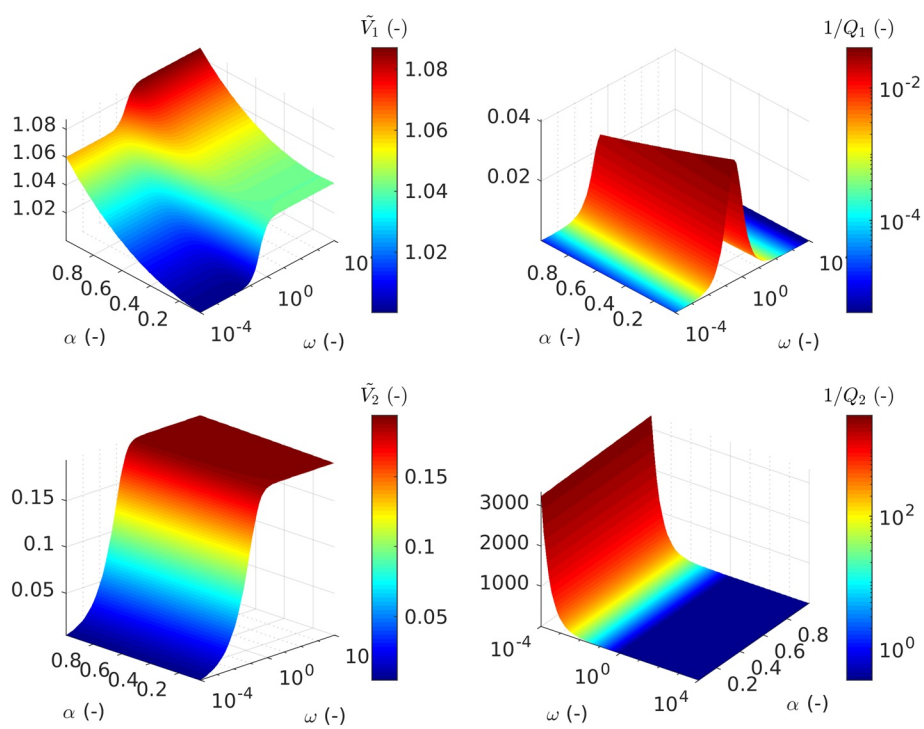

Figure 3. Non-dimensional phase velocities ($\tilde{V}_1$ and $\tilde{V}_2$) and the corresponding quality factors ($1/Q_1$ and $1/Q_2$) as a function of the non-dimensional Biot-Willis coefficient α and the non-dimensional angular frequency ω. The material parameters are those from Table 3.

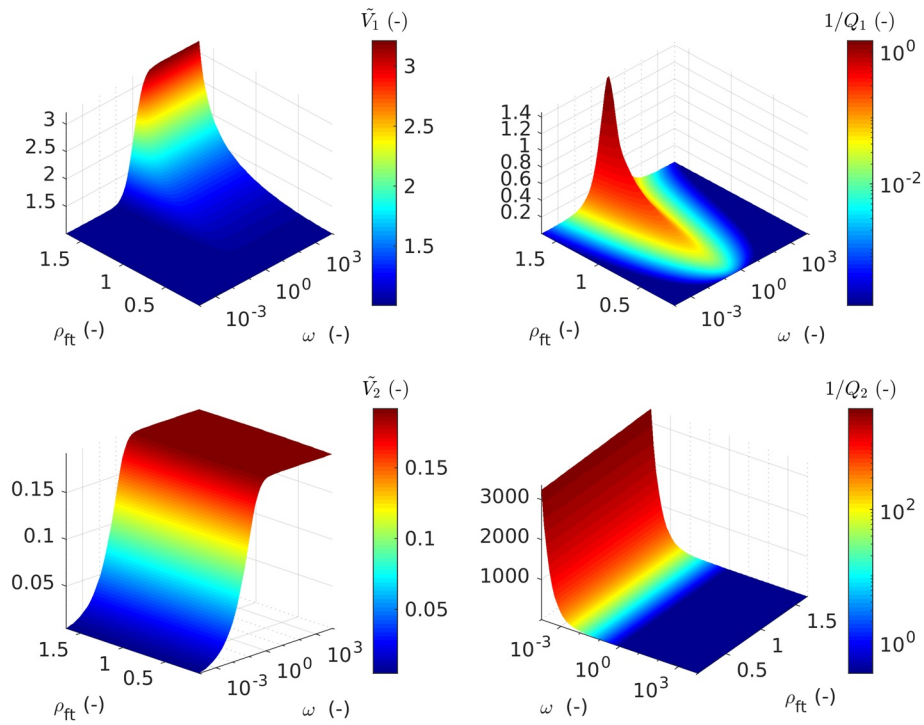

Figure 4. Non-dimensional phase velocities ($\tilde{V}_1$ and $\tilde{V}_2$) and the corresponding quality factors ($1/Q_1$ and $1/Q_2$) as a function of the non-dimensional parameter ρ_{ft} and the non-dimensional angular frequency ω. The material parameters are those from Table 3.

(Figures 4a and 4b), while at low frequencies ($\omega \in [10^{-4}, 10^{-1}]$), $\tilde{V}_1$ is independent on ρ_{ft} (Figure 4a). $\tilde{V}_2$ and $1/Q_2$ are almost independent on ρ_{ft} in the whole frequency range (Figures 4c and 4d).

4. Numerical Implementation of the Elastodynamic Biot's Equations

We solve the first order velocity-stress formulation of the elastodynamic Biot's Equations 1–8 on a rectangular time-space grid. We base our approach on a conservative staggered space-time grid discretization (Virieux, 1986); for Darcy's flux, we use a semi-implicit discretization (Alkhimenkov et al., 2020). A conservative staggered space-time grid discretization is equivalent to a finite volume approach (Dormy & Tarantola, 1995) (see also LeVeque (1992)). This approach follows from the early Marker and Cell (MAC) method which is a classical method in computational fluid dynamics (Harlow & Welch, 1965; McKee et al., 2008). Field variables are located either at the cell center or corners and, fluxes are computed at the cell boundaries resulting in a conservative staggered grid formulation. Other similar methods were developed such as the standard staggered grid scheme (Levander, 1988; Virieux, 1986; Virieux & Madariaga, 1982), the rotated staggered grid scheme (Saenger et al., 2000), and the Lebedev scheme (Davydycheva et al., 2003; Lebedev, 1964; Lisitsa & Vishnevskiy, 2010). The elastodynamic Biot's equations using the standard staggered grid scheme were solved by Masson et al. (2006). Moczo et al. (2007) provides a review on staggered finite-difference methods for wave propagation in elastic media.

4.1. The First Order Elastodynamic Biot's Equations with a Volumetric-Deviatoric Split

Numerically solving the elastodynamic Biot's Equations 1 and 8 requires the coefficient matrices in 1 and 8 to be inverted. This formulation leads to a system of equations describing poroelastic wave propagation in three-dimensional media and can be solved explicitly:

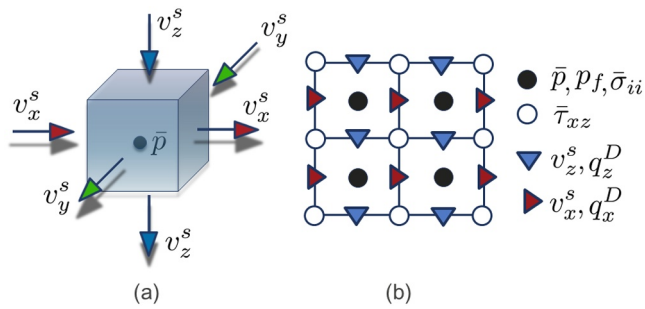

Figure 5. A sketch representing (a) the finite volume, where the solid velocities preserve mass balance and (b) the spatial positions of different fields in the X–Z plane. Darcy's fluxes obey the same behavior.

$$\begin{pmatrix} \dfrac{\partial \bar{p}}{\partial t} \\ \dfrac{\partial p_f}{\partial t} \end{pmatrix} = -K_u \begin{pmatrix} 1 & B \\ B & \dfrac{B}{\alpha} \end{pmatrix} \begin{pmatrix} \nabla_k v_k^s \\ \nabla_k q_k^D \end{pmatrix}, \tag{41}$$

$$\frac{\partial \bar{\tau}_{ij}}{\partial t} = 2G\left(\frac{1}{2}(\nabla_i v_j^s + \nabla_j v_i^s) - \frac{1}{3}(\nabla_k v_k^s)\delta_{ij}\right) \tag{42}$$

and

$$\begin{pmatrix} \dfrac{\partial v_i^s}{\partial t} \\ -\dfrac{\partial q_i^D}{\partial t} \end{pmatrix} = \frac{1}{\Theta}\begin{pmatrix} \rho_a & \rho_f \\ \rho_f & \rho_t \end{pmatrix} \begin{pmatrix} \nabla_j\left(-\bar{p}\delta_{ij} + \bar{\tau}_{ij}\right) \\ \dfrac{\eta_f}{k} q_i^D + \nabla_i p_f \end{pmatrix}, \tag{43}$$

where $\Theta = \rho_t \rho_a - \rho_f^2$. Note that the coefficient matrices in Equations 41 and 43 are symmetric by analogy Equations 1 and 8. Symmetry combined to non-dimensional analysis is a requirement that allows us to derive a time stepping condition in the explicit form.

4.2. Discretization

The numerical implementation consists of a time evolution operator to perform time steps within a time loop and space operators to relate fields at old and new times. We rely on a rectangular time-space grid. The time discretization is $t^l = l\Delta t$ and the spatial grid is $x_i = i\Delta x$, $y_j = j\Delta y$, and $z_k = k\Delta z$. The velocity vector field and the Darcy's flux are defined at half-integer spatial nodes and integer time nodes:

$$(v_x^s)^l_{i+1/2,j,k}, (v_y^s)^l_{i,j+1/2,k}, (v_z^s)^l_{i,j,k+1/2}, (q_x^D)^l_{i+1/2,j,k}, (q_y^D)^l_{i,j+1/2,k}, (q_z^D)^l_{i,j,k+1/2}. \tag{44}$$

The total and fluid pressure scalar fields are defined at integer spatial nodes and half-integer time nodes: $(\bar{p})^{l+1/2}_{i,j,k}, (p_f)^{l+1/2}_{i,j,k}$. The stress deviator tensor fields are defined as $(\bar{\tau}_{xy})^{l+1/2}_{i+1/2,j+1/2,k}, (\bar{\tau}_{xz})^{l+1/2}_{i+1/2,j,k+1/2}, (\bar{\tau}_{yz})^{l+1/2}_{i,j+1/2,k+1/2}$. A schematic representation of spatial positions is shown in Figure 5. The proposed discrete scheme is second order accurate in space and time. The material parameters are constant inside the finite volumes and may be discontinuous between them. The discrete operators for Biot's Equations 41–43 are given in Appendix E.

4.3. Stiffness of Biot's Equations

Wave propagation and fluid pressure diffusion in poroelastic media occur simultaneously but feature very different time scales. This phenomenon is called stiffness of the Biot's equations (e.g., Carcione and Quiroga-Goode (1995)). Stiffness of an equation is a serious issue for numerical solutions because the discrete time step may drop to values hindering the numerical simulation to complete. A simple solution exist to circumvent this issue for Biot's equations (Alkhimenkov et al., 2020; Masson et al., 2006), briefly reported here. The one-dimensional discrete version of 43 is

$$\begin{cases} -\dfrac{[q^D]^{l+1}_{i+1/2} - [q^D]^l_{i+1/2}}{\Delta t} = \dfrac{\rho_f}{\Theta}\dfrac{[\bar{\sigma}]^{l+1/2}_{i+1} - [\bar{\sigma}]^{l+1/2}_i}{\Delta x} \\ +\dfrac{\rho_t}{\Theta}\left(\dfrac{[p_f]^{l+1/2}_{i+1} - [p_f]^{l+1/2}_i}{\Delta x} + \dfrac{\eta_f}{k}\left(\chi[q^D]^{l+1}_{i+1/2} + (1-\chi)[q^D]^l_{i+1/2}\right)\right) \\ \dfrac{[v^s]^{l+1}_{i+1/2} - [v^s]^l_{i+1/2}}{\Delta t} = \dfrac{\rho_a}{\Theta}\dfrac{[\bar{\sigma}]^{l+1/2}_{i+1} - [\bar{\sigma}]^{l+1/2}_i}{\Delta x} \\ +\dfrac{\rho_f}{\Theta}\left(\dfrac{[p_f]^{l+1/2}_{i+1} - [p_f]^{l+1/2}_i}{\Delta x} + \dfrac{\eta_f}{k}\left(\chi[q^D]^{l+1}_{i+1/2} + (1-\chi)[q^D]^l_{i+1/2}\right)\right) \end{cases} \tag{45}$$

The weight parameter χ plays the key role in the numerical solution of Biot's equations. The case $\chi = 0$ corresponds to a fully explicit scheme; calculating $[q^D]^{l+1/2}$ (45) only requires $[q^D]^{l-1/2}$. In this case, the stable time step becomes very small due to the stiffness of Biot's equations. The opposite end-member $\chi = 1$ corresponds to an implicit scheme where the stiffness no longer affects the time step stability; calculating $[q^D]^{l+1/2}$ (45) requires $[q^D]^{l+1/2}$. Since Biot's equations do not contain spatial derivatives of the Darcy's flux q_x^D in 45, the implicit scheme $\chi = 1$ can be achieved in an iterative fashion (i.e., updates in the iteration loop are explicit). The one dimensional code for $\chi = 1/2$ is shown in Figure 7. The weight parameter χ plays the key role in the stability and convergence rate of the numerical scheme which is explored in the next section.

4.4. Von Neumann Stability Analysis

The von Neumann stability method analyzes a time evolution of a discrete numerical solution of a given PDE. The method provides the stability of linear schemes with constant coefficients. We here summarize the von Neumann stability analysis' main results (Alkhimenkov et al., 2020) for Biot's poroelastic equations' discrete scheme (see also Masson et al. (2006)). For that let us introduce the matrices of coefficients

$$\zeta_{ij} = \begin{pmatrix} \zeta_{11} & \zeta_{12} \\ \zeta_{21} & \zeta_{22} \end{pmatrix} = \begin{pmatrix} K_u + 4/3G & \alpha M \\ \alpha M & M \end{pmatrix} \tag{46}$$

and

$$\varrho_{ij} = \begin{pmatrix} \varrho_{11} & \varrho_{12} \\ \varrho_{21} & \varrho_{22} \end{pmatrix} = \frac{1}{\Theta}\begin{pmatrix} \rho_a & \rho_f \\ \rho_f & \rho_t \end{pmatrix}, \tag{47}$$

the parameter Θ is already defined in 43. The determinants of these matrices are

$$\det(\zeta_{ij}) = \zeta_{11}\zeta_{22} - \zeta_{12}^2, \det(\varrho_{ij}) = \varrho_{11}\varrho_{22} - \varrho_{12}^2, \tag{48}$$

and the Hadamard product (element-wise multiplication) of ζ_{ij} and ϱ_{ij} is

$$h_{ij} \equiv (\zeta \circ \varrho)_{ij} = \begin{pmatrix} \zeta_{11}\varrho_{11} & \zeta_{12}\varrho_{12} \\ \zeta_{21}\varrho_{21} & \zeta_{22}\varrho_{22} \end{pmatrix}. \tag{49}$$

The parameter A is defined as

$$A = h_{11} + h_{22} - 2h_{12} \tag{50}$$

By using (48) and (50), the fast wave phase velocity in the high-frequency limit V_1^{HF} can be calculated as

$$V_1^{HF} = \left(\frac{A - \sqrt{A^2 - 4\det(\zeta_{ij})\det(\varrho_{ij})}}{2\det(\zeta_{ij})\det(\varrho_{ij})} \right)^{-1/2}. \tag{51}$$

The matrices ζ_{ij}, ϱ_{ij}, and $\eta_k \equiv \eta/k$ fully describe the dimensional elastodynamic Biot's Equations 41–43. The main issue with the numerical modeling of the Biot's equations is the treatment of the parabolic operator in (Equation E14) and (Equation E15). If $\eta_k = 0$, then the system (41)–(43) corresponds to the two coupled hyperbolic equations, having two longitudinal waves. The stability analysis shows that the Courant-Friedrichs-Lewy (CFL) condition for such system is $\Delta t \leqslant \Delta x / V_1^{HF}$ (Alkhimenkov et al., 2020), where V_1^{HF} is given by expression (51).

If $\eta_k \neq 0$ and $\chi = 0$, then the parabolic operator $\overline{D}_\chi[q_f^D]$ in (Equation E14) and (Equation E15) affects stability and the system of equations becomes stiff. If η_k reaches a certain value, the stable time step Δt dramatically decreases as a function of η_k (Figure 6a). The increase in porosity ϕ also reduces Δt but this

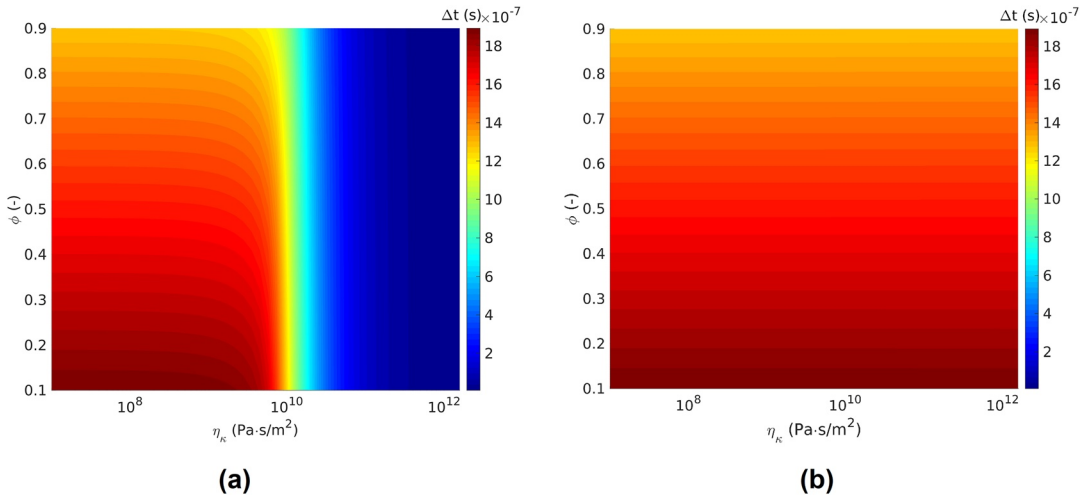

Figure 6. The von Neumann stability analysis for the elastodynamic Biot's Equations 41–43 as a function of $\eta_k = \eta/k$ and porosity ϕ. Panel (a) corresponds to the $\chi = 0$ scheme and panel (b) corresponds to the $\chi = 1/2$ scheme. The stability of the $\chi = 1$ scheme is identical to that one of the $\chi = 1/2$ scheme. The material parameters are those from Table 3.

reduction is small compared to the reduction due to the increase of η_k. However, for the $\chi = 1/2$ scheme or $\chi = 1$ scheme, the parameter η_k does not affect the stable time step Δt (Figure 6b). In this case, the parabolic operator $\bar{D}_\chi[q_f^D]$ is calculated implicitly, thus, the CFL condition is not affected by η_k. The $\chi = 1/2$ or $\chi = 1$ schemes are stable in one space dimension under the CFL condition

$$\Delta t \leqslant \frac{\Delta x}{V_1^{HF}}, \tag{52}$$

where the expression for V_1^{HF} is given by Equation 51, which is the same as for the inviscid case. The $\chi = 1/2$ scheme is more preferable than the $\chi = 1$ scheme, since the $\chi = 1/2$ scheme provides a second order accuracy, which is explored below.

For any considered above schemes, the matrices ζ_{ij} and ϱ_{ij} must be positive definite as well in order to preserve hyperbolicity of the system (Alkhimenkov et al., 2020). The positive definiteness of the matrix in Equation 41 and ϱ_{ij} also follows from physics, for example, from the classical irreversible thermodynamics (Jou et al., 2001; Yarushina & Podladchikov, 2015). Note, that the positive definiteness of the matrix in Equation 41 is a more restrictive condition than the positive definiteness of ζ_{ij} (46) and are the same if the shear modulus G is zero.

The extension of the CFL condition (52) to the two, three and n-dimensions is straightforward

$$\Delta t \leqslant \frac{1}{V_1^{HF}\sqrt{\sum_{i=1}^{n}\frac{1}{\Delta x_i^2}}}. \tag{53}$$

If $\Delta x_i = \Delta x$, then

$$\Delta t \leqslant \frac{\Delta x}{\sqrt{n}\,V_1^{HF}}. \tag{54}$$

The conditions (52)–(54) can be generalized to a fourth-order accurate in space, second-order accurate in time numerical scheme using the coefficients of the fourth-order approximation to the first derivative (Levander, 1988; Masson et al., 2006).

```
Prf          = exp(-(x/lamx).^2); chi = 0.5;
for it = 1:nt
    stress_xx   = stress_xx  + ( zeta_11.*diff(Vx,1,1)/dx + zeta_12.*diff(Qx,1,1)/dx)*dt;
    Prf         = Prf        - ( zeta_21.*diff(Vx,1,1)/dx + zeta_22.*diff(Qx,1,1)/dx)*dt;
    Qx_old      = Qx;
    Qx(2:end-1) = (Qx(2:end-1)/dt - diff(stress_xx,1,1)/dx.*varrho_21 - (diff(Prf,1,1)/dx +...
          (1-chi).*Qx(2:end-1) .*etaf_k).*varrho_22)./(1/dt + chi.*varrho_22.*etaf_k);
    Vx(2:end-1) = (Vx(2:end-1)/dt + diff(stress_xx,1,1)/dx.*varrho_11 + (diff(Prf,1,1)/dx +...
             (chi.*Qx(2:end-1) + (1-chi).*Qx_old(2:end-1)).*etaf_k).*varrho_12)*dt;
end
```

Figure 7. The one dimensional code using the proposed scheme with $\chi = 1/2$ in MATLAB. The initial condition of the Gaussian form is set to the fluid pressure. zeta_ij are the matrix coefficients ζ_{ij} in Equation 46, varrho_ij are the matrix coefficients ϱ_{ij} in Equation 47, etaf_k corresponds to η/k, chi corresponds to χ, lamx stands for l_x, stress_xx stands for $\bar{\sigma}_{xx}$, Prf stands for p_f, Qx stands for q_x^D, and Vx stands for v_x^s.

4.5. Sources, Initial and Boundary Conditions

We initialize the majority of our simulations with a Gaussian perturbation,

$$F_G = A_0\, e^{-(x/l_x)^2-(y/l_y)^2-(z/l_z)^2}, \tag{55}$$

where x, y, and z are the arrays of spatial coordinates, l_x, l_y, and l_z are the parameters controlling the shape (width) of the Gaussian and A_0 defines its amplitude. We set l_x, l_y, and l_z as a certain fraction of the domain extend.

Depending on the model configuration, we implemented two types of sources in the right-hand side of the total pressure (isotropic media) or total stress (anisotropic media) equation (see Appendix D for the full set of equations). The first type of source is the Morlet wavelet

$$F_M(t) = \mathrm{Re}\left[(\pi f_b)^{-1/2} e^{\left(2\pi i f_c (t-t_0)\right)} e^{-(t-t_0)^2/f_b}\right] = (\pi f_b)^{-1/2} cos\left(2\pi f_c (t-t_0)\right) e^{-(t-t_0)^2/f_b} \tag{56}$$

and the second type of source is the Ricker wavelet

$$F_R(t) = \left(1 - 2\left(\pi(t-t_0) f_c\right)^2 e^{-\left(\pi(t-t_0) f_c\right)^2}, \tag{57}$$

where f_c is the the source peak frequency, t is time, t_0 is the wavelet delay, and f_b is the time-decay parameter of the Morlet wavelet. The Morlet wavelet features a distinct narrow bandwidth in the frequency domain which significantly reduce the wavelet shape changes during the pulse propagation in a lossy medium. The disadvantage results in a significant time spread in time domain. We use reflecting boundary conditions in our simulations.

The one-dimensional time loop implementation of the proposed scheme (Equation E8–E15) in MATLAB (R2018a) using the Gaussian initial condition (55) is shown in Figure 7.

5. Multi-GPU Implementation

GPUs are many-core processors originally designed to refresh screen pixels at very high frame-rates for computer games. Nowadays, GPUs are widely used in high-resolution numerical modeling due to their ability to efficiently execute a large number of operations simultaneously. Several studies focused on the implementation of wave propagation solvers using GPUs (Komatitsch et al., 2010; Mehra et al., 2012; Michéa & Komatitsch, 2010; Rubio et al., 2014; Weiss & Shragge, 2013). The CUDA extension to the C language (CUDA, 2020) makes it possible to write C-style codes that are executed in parallel on GPUs. A brief description of the GPU architecture is given in Appendix F.

a)

```
init<<<grid,block>>>(Prf, sigma_xx, sigma_yy, sigma_zz, Vx, Vy, Vz, ...);
cudaDeviceSynchronize();

for (it=0;it<nt;it++)
{
    compute_StressPrf<<<grid,block>>>(Prf, sigma_xx, sigma_yy, sigma_zz, ...);
    cudaDeviceSynchronize();

    swap(Qxold,Qx); swap(Qyold,Qy); swap(Qzold,Qz);
    cudaDeviceSynchronize();

    update_QV<<<grid,block>>>(Vx, Vy, Vz, Qxft, Qyft, Qzft, ...);
    cudaDeviceSynchronize();
}
```

b)

```
init<<<grid,block>>>(Prf, sigma_xx, sigma_yy, sigma_zz, Vx, Vy, Vz, ...);
cudaDeviceSynchronize();

for (it=0;it<nt;it++)
{
    compute_StressPrf<<<grid,block>>>(Prf, sigma_xx, sigma_yy, sigma_zz, ...);
    cudaDeviceSynchronize();

    swap(Qxold,Qx); swap(Qyold,Qy); swap(Qzold,Qz);
    cudaDeviceSynchronize();

    for (istep=0; istep<2; istep++)
    {
        update_QV<<<grid,block,0,streams[istep]>>>(Vx, Vy, Vz, Qxft, Qyft, Qzft, ...);
        update_sides3(Qx,nx+1,ny,nz, Qy,nx,ny+1,nz, Qz,nx,ny,nz+1)
        update_sides3(Vx,nx+1,ny,nz, Vy,nx,ny+1,nz, Vz,nx,ny,nz+1)
    }
    cudaDeviceSynchronize();
}
```

Figure 8. Time loop computations for (a) a single GPU CUDA C code and (b) a multi-GPUs CUDA C code implementation. compute_StressPrf corresponds to the update of all stresses $\overline{\sigma}_{ij}$ and fluid pressure p_f. update_QV corresponds to the update of velocities v_i^s and Darcy fluxes q_i^D swap (...) stands for a pointer swap of Darcy's fluxes between old and new values.

5.1. Computing Systems

We calculated our results on various computing systems depending mainly on the targeted numerical resolution. We performed most of our simulations on an Nvidia DGX-1 - like node hosting 8 Nvidia Tesla V100 Nvlink (32 GB) GPUs, 2 Intel Xeon Silver 4112 (2.6 GHz) CPUs, and 768 GB DDR4 RAM. The second computing system hosts a single Nvidia Tesla V100 PCIe (16 GB) GPU, 2 Intel XEON E5-2620V2 4112 (2.1 GHz) CPUs, and 64 GB DDR3 RAM. The third computing system is composed of 32 nodes, each featuring 4 Nvidia GeForce GTX Titan X Maxwell (12 GB) GPUs, 2 Intel XEON E5-2620V3 4112 (2.4 GHz) CPUs, and 128 GB DDR4 RAM.

5.2. Code Implementation on a Single GPU

The CUDA C code structure (Figure 8a) is similar to the MATLAB one (Figure 7). The time loop calls two kernels – or GPU functions – to sequentially update all stresses and the fluid pressure and then update the fluid and solid velocities. Darcy's fluxes q_x^D, q_y^D, q_z^D are time-dependent fields present in both Equation E14 and Equation E15 exhibiting history or time dependence that require them to be stored from previous iteration. We perform the update relying on a pointer swap at every iteration to prevent race conditions and to avoid copying the array itself, which would significantly deprecate the performance. To reduce redundant memory accesses, we locally precompute and store corresponding field variables. In the compute_StressPrF() kernel, we store the derivatives of the velocities v_i^s and Darcy fluxes q_i^D. In the Update_QV () kernel, we store derivatives of stresses $\overline{\sigma}_{ij}$ and fluid pressure p_f.

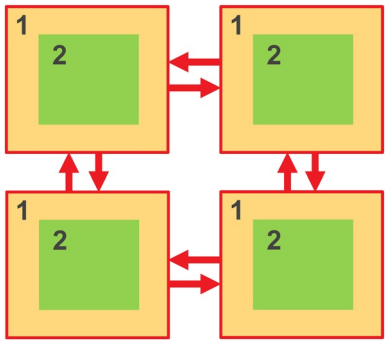

Figure 9. Schematic representation of a domain decomposition on four GPUs. First, the computation of the boundary points (1) of the local domains using streams is performed, then the computation of the inner points (2) of the local domains is carried out together with the non-blocking MPI messages to exchange the boundary values (represented by red boundary lines) among neighboring GPU units. GPU, Graphical processing units; MPI, message passing interface.

5.3. The Multi-GPU Code Implementation

The single GPU code enables thousands of threads to simultaneously compute physics on every grid points of the computational domain in a shared (GPU) memory approach. To overcome the on-GPU DRAM memory limitation and leverage the simultaneous utilization of multiple GPUs we implemented a distributed memory parallelization using the message passing interface (MPI) standard. The parallelization among multiple GPUs requires the exchange of the internal boundary values of the solid velocities v^s and the Darcy's fluxes q^D (represented by black lines in Figure 9). Global boundary conditions are applied if the local sub-domains coincide with the global domain boundaries. We rely on CUDA-aware non-blocking MPI messages for internal boundary condition updates among neighboring GPUs. The CUDA-awareness implies that GPU device pointers can directly be exchanged with MPI bypassing a local CPU copy on both sender and receiver side.

We implemented an overlap among computation and MPI communication to avoid a drop in performance with an increase in the number of MPI processes (Räss, Omlin, & Podladchikov, 2019). Only minimal changes are required to implement this computation/communication overlap and fully hide the MPI boundary exchange latency (Figure 8b). We divided the local computational domain on each GPU in two parts, a boundary points region (1 in Figure 9) and an inner points region (2 in Figure 9). We then use CUDA Streams to perform an asynchronous kernel call in an iterative fashion using two distinct execution pipelines (Räss, Omlin, & Podladchikov, 2019). The first update kernel call computes the boundary flagged nodes only and executes on the high priority stream. Then, the MPI boundary updates starts on the same high priority stream (the update_sides3 function). In the meanwhile, the update kernel call is executed a second time within the istep loop, now flagging and computing the remaining inner points. A wise definition of the number of grid points to include (i.e., the boundary width) enables optimal performance results.

The Nvidia visual profiler (nvvp) is an informative tool to visualize the execution timeline of a GPU process (Figure 10). We compare multi-GPU codes without (Figure 10a) and with (Figure 10b) computation/communication overlap running on an eight GPUs (information shown only for two GPUs). The visual timeline depicts the q^D and v^s boundary points update on the high priority CUDA stream 21 followed by the MPI message sending and receiving among GPUs (the time line is shown by red box in Figure 10b). During the same time, the q^D and v^s inner points update happens on the lower priority CUDA stream 22. The update kernel is executed two times (green boxes in Figure 10b). The cumulative time of the sequential executions is identical to the unsplit execution time (Figures 10a and 10b).

5.4. Performance Benchmark

We assess the solver's performance and realize the weak scaling tests in a similar fashion as proposed by Räss, Duretz, and Podladchikov (2019); Duretz et al. (2019); Räss et al. (2020). These studies highlight the memory-bounded nature (in opposition to compute-bounded) of a waste majority of PDE solver implementations nowadays on many-core (e.g., GPU) hardware; Memory transfers are limiting the performance of an application, while floating point (arithmetic) operations are not performance relevant. We therefore focus on the memory access efficiency in our numerical calculations. The effective memory throughput ($\mathrm{MTP}_{\mathrm{effective}}$) metric (Omlin, 2016; Omlin et al., 2020) evaluates how efficiently data is transferred between the memory and the computation units, in gigabytes per second (GB/s):

$$\mathrm{MTP}_{\mathrm{effective}} = \frac{n_x \times n_y \times n_z \times n_t \times n_{\mathrm{IO}} \times n_{\mathrm{p}}}{10^9 \times t_{n_t}}, \tag{58}$$

where n_x, n_y, and n_z are the number of grid cells, n_t is the number of iterations, n_{IO} is the number of read and write memory accesses (the least value needed to solve the problem for the chosen numerical

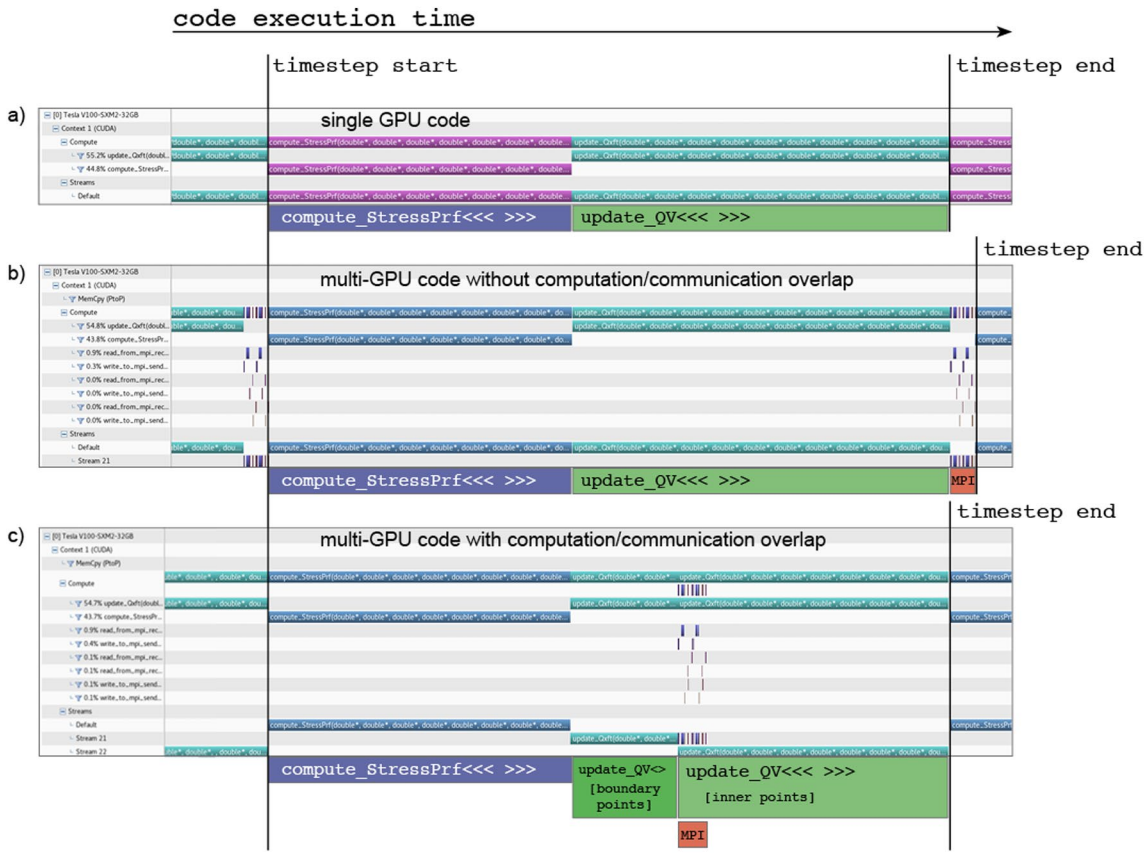

Figure 10. The Nvidia visual profiler (nvvp) output for various GPU code implementations: (a) single GPU (without computation/communication overlap), (b) mulit-GPUs (without computation/communication overlap), and (c) multi-GPUs (with computation/communication overlap). All implementations share the same compute_StressPrf kernel. The update_QV kernel is (a) executed once per time step updating both boundary and inner points, (b) executed once per time step and followed by internal boundary exchange using MPI, and (c) executed in a serial fashion, first updating the boundary points, then internal boundary exchange occurs using MPI while the inner points are asynchronously computed in the second call of the update_QV kernel. The computation/communication overlap referred to as computational split involves 48, 16, and 16 grid cells in in x-, y-, and z-directions, respectively. GPU, Graphical processing units; MPI, message passing interface; nvvp, Nvidia visual profiler.

scheme), n_p is the floating-point arithmetic precision (either four or eight bytes) and t_{n_t} is the time (in seconds) needed to perform the n_t iterations. The closer the value of $\mathrm{MTP}_{\mathrm{effective}}$ gets to the memory copy only value, the better the performance is. We carried out all the performance tests on the anisotropic Biot 3D implementation using the $\chi = 1/2$ scheme and scalar material properties (see Appendix D for the full set of equations). In that case $n_{\mathrm{IO}} = 42$. We used a numerical spatial resolution of 576^3 grid cells on a Tesla V100 32 GB Nvlink GPU, allocating 29 GB on-chip DRAM memory. We used a numerical spatial resolution of $511 \times 511 \times 127$ grid cells on the Titan X (Maxwell) 12 GB GPU allocating 5 GB on-chip DRAM memory. The maximum global domain spatial resolution on 128 Titan X (Maxwell) 12 GB GPUs involved 4.5 billion grid cells.

5.4.1. Benchmark Results for a Single GPU Implementation

Figure 11 depicts the effective memory throughput (MTP) of the Biot 3D numerical application as a function of the number of threads per blocks in x-, y-, and z-direction on a Tesla V100 32 GB Nvlink GPU. The $\mathrm{MTP}_{\mathrm{ref}}$ corresponds to the reference MTP, that is, the best combination of threads per blocks (32, 2, 16) for a given resolution of 576^3; the MTP of all simulations ($\mathrm{MTP}_{\mathrm{effective}}$) are normalized by $\mathrm{MTP}_{\mathrm{ref}}$. The maximal performance drop from the reference MTP is about 17%. It is interesting, that the (32, 2, 8) combination uses only 512 threads out of the 1,024 available but shows almost the same performance as combinations involving 1,024 threads. Good performance with under-utilization of the threads per block resources is known and may result by the increase in the number of concurrent blocks launched allowing for optimal scheduling.

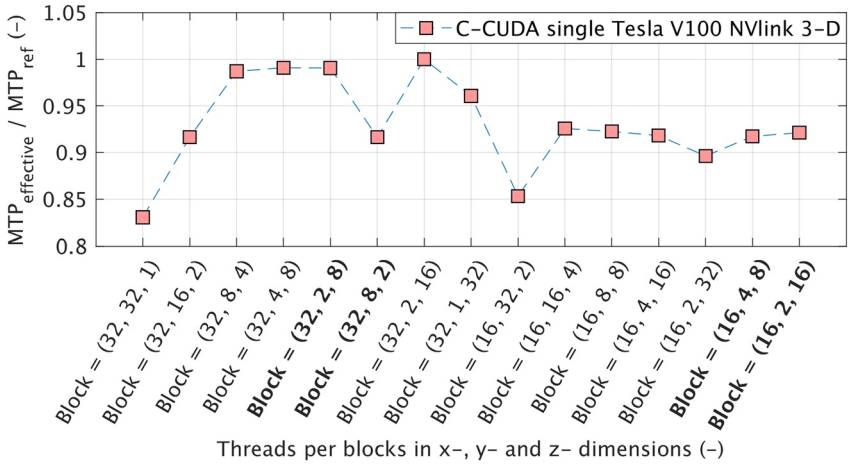

Figure 11. The effective memory throughput as a function of the number of threads per blocks (in x-, y-, and z-direction). The MTP of all simulations ($MTP_{effective}$) are normalized by MTP_{ref} (corresponds to Block (32, 2, 16)). The bold color corresponds to thread-block combinations of 512 threads out of the 1,024 available. MTP, memory throughput.

Figure 12 shows memory access efficiently between the GPU global memory and the computation units as a function of on-chip RAM memory. Our 3D numerical application achieves on average 90% of the "ideal" memory copy only efficiency (copying two 3D arrays without performing any calculations, 740 GB/s) on a single Tesla V100 32 GB NVlink GPU. The average performance is 660 GB/s. A huge drop in the memory access performance at low on-chip RAM memory utilization reflects computations without enough data to saturate the memory bandwidth.

We additionally assessed the effective memory throughput of our 3D routine on a Tesla V100-SXM2 16 GB accessed on the Amazon Elastic Compute Cloud environment (Amazon EC2); our 3D routine performs on average at 740 GB/s (memory copy at 795 GB/s) validating the benchmark results obtained on our local GPU cluster. The discrepancy we observe may be caused by different versions of Nvidia drivers and compilers.

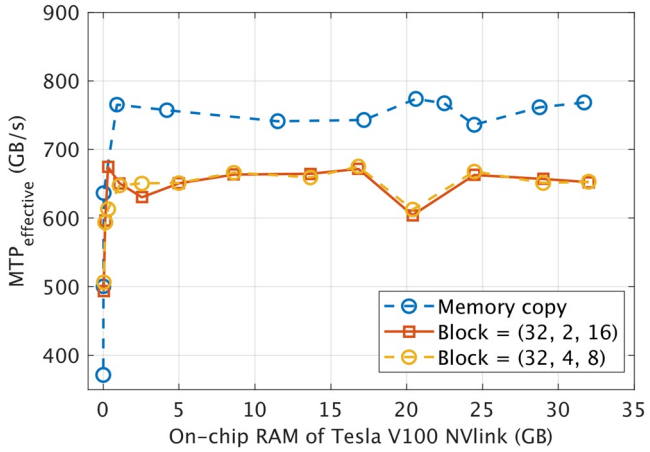

Figure 12. The memory access efficiently as a function of the allocated on-chip DRAM memory. The blue curve corresponds to the "ideal" memory copy efficiency (copying two 3D arrays without performing any calculations), red and yellow curves represent the memory copy efficiency involving all the physics, which is on average 90% of the "ideal" memory copy efficiency.

5.4.2. Benchmark Results for a Multi-GPU Implementation

We further investigate the influence of the boundary width on the performance (Figure 13). The split among computation domains allowing for overlap of computation and communication affects the performance. Considering too few or too many boundary points hinders optimal kernel execution as too few resources may be used in the first or the second sequential call. The code execution on a single Tesla V100 GPU with boundary width ratios of 0.2–0.8 returns equivalent performance as the execution without the computational split. The performance of the code on 8 Tesla V100 GPUs including MPI communication shows a 2% performance drop compared to the single GPU process. We achieved the best performance using approximately a ratio of 0.3 between boundary and inner points. This splitting allows for enough data to keep all threads busy during the boundary point calculation (the first kernel execution) and provides sufficient time to hide the MPI message sent during the update of the inner points (the second kernel execution).

We performed a weak scaling test using the 1–8 Tesla V100 32 GB NVlink GPUs and the 1–128 Titan X 12 GB GPUs (Figure 14). The parallel efficiency of 1–8 GPUs is 98% and on average 96% on 16–128 Titan X GPUs with a standard deviation of 2%. A standard deviation was calculated as a result of ten simulations. We globally achieved a performance of about 5,280 GB/s on 8 Tesla V100 32 GB NVlink GPUs. Such performance im-

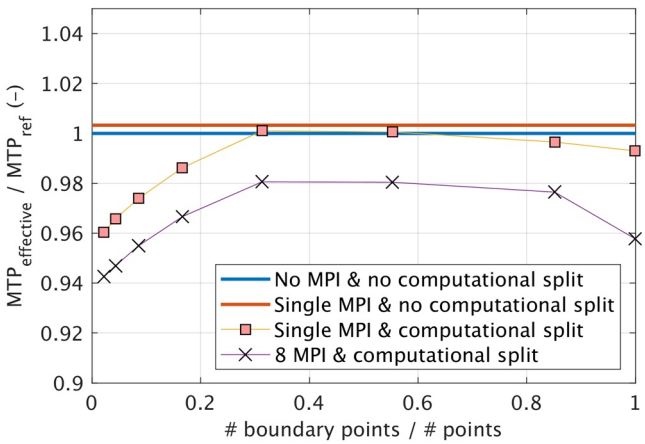

Figure 13. The impact of the boundary width on the memory access efficiency. All the performance results are normalized by MTP_{ref} of the non-MPI code implementation. MPI, message passing interface; MTP, memory throughput.

plies that only 95 s are needed to perform 1,000 (double-precision) explicit time iterations of a model involving 1.5 billion grid cells (1152^3).

5.5. Validation of the Numerical Solver

5.5.1. Comparison Against an Analytical Solution

We perform a direct comparison of our numerical solver against analytically derived non-dimensional phase velocities and the inverse quality factors of 1D Biot's equations in homogeneous poroelastic media. Biot's mechanism, often called global flow, is the unique cause leading to wave attenuation and velocity dispersion. We validated our numerical solver in 1D but the plane wave analysis is multidimensional as plane wave characteristics are identical in 1D, 2D, and 3D. In the numerical simulation, we use the proposed scheme (Equation E8–E15) with $\chi = 1/2$, the Morlet wavelet as a source function (56) and quantify velocity and the inverse of the quality factor of a propagating wavelet in the time domain. We obtain excellent agreement between numerical and analytical results (Figure 15).

5.5.2. Convergence Analysis

We performed a grid convergence analysis to validate the numerical implementation of the solver. We evaluate the magnitude of the phase velocity truncation errors (e_V) as functions of decreasing spatial discretization steps Δx. We calculate the truncation errors by subtracting numerically calculated fields from analytical fields and characterize the magnitude of the truncation errors by their L_1 norms, using the velocity estimation (Räss et al., 2017)

$$e_V = \left\| V_a - V_n \right\|_1, \tag{59}$$

where V_a corresponds to the analytical velocity obtained via the dispersion analysis and V_n corresponds to the numerically estimated velocity.

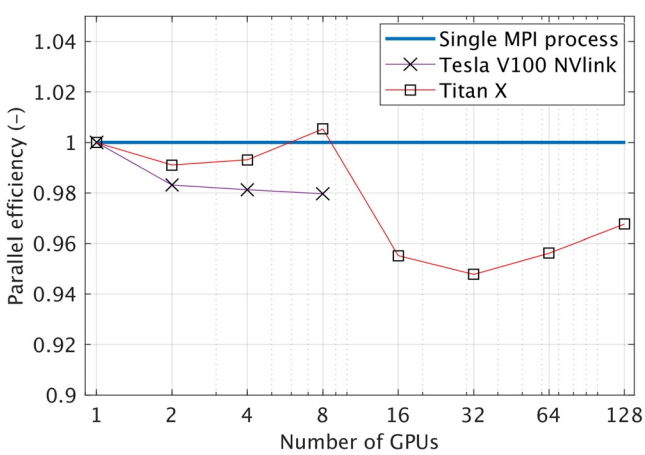

Figure 14. The MPI weak scaling tests of the anisotropic Biot 3D implementation. We show the parallel efficiency of the two Nvidia hardware accelerators, the 1–8 Tesla V100 32 GB NVlink GPUs (Volta) and the 1–128 Titan X 12 GB GPUs (Maxwell). All the performance results are normalized by the single-MPI code performance. MPI, message passing interface.

Figure 16a shows the truncation error magnitudes of the estimated velocity in a lossless ($\eta/k = 0$) and lossy ($\eta/k \neq 0$) media using the $\chi = 1/2$ scheme (Equation E8–E15). The source has the form of a Ricker wavelet (57) and the central frequency of the source corresponds to a very low frequency (much lower than the frequency of $1/Q$ maximum). Our numerical solutions for velocity exhibits second-order spatial and temporal accuracy. The truncation error magnitudes decrease by a factor k as the grid spacing is reduced by the same factor. We obtain similar results for a very high frequency source (much higher central frequency than the frequency of $1/Q$ maximum).

Figure 16b shows the truncation error magnitudes of the estimated velocity in a lossy medium for the scheme (Equation E8–E15) with $\chi = 1/2$ and $\chi = 1.0$. Here, the central frequency of the source corresponds to the frequency of $1/Q$ maximum. In this analysis, we use the numerically estimated velocity of a very high resolution simulation. The $\chi = 1/2$ scheme exhibits second-order accuracy in space and in time. In contrast, the $\chi = 1.0$ scheme shows only about 1.8 order accuracy. Only the $\chi = 1/2$ scheme exhibits second-order spatial and temporal accuracy across all frequencies while the $\chi = 1.0$ scheme exhibit second-order spatial and temporal accuracy only at low or high frequencies where attenuation (and dispersion) is very low. For schemes with χ other than 1/2 (we used $\chi = 0.6$, 0.7, 0.8, and 0.9), tests show that the accuracy is lower than sec-

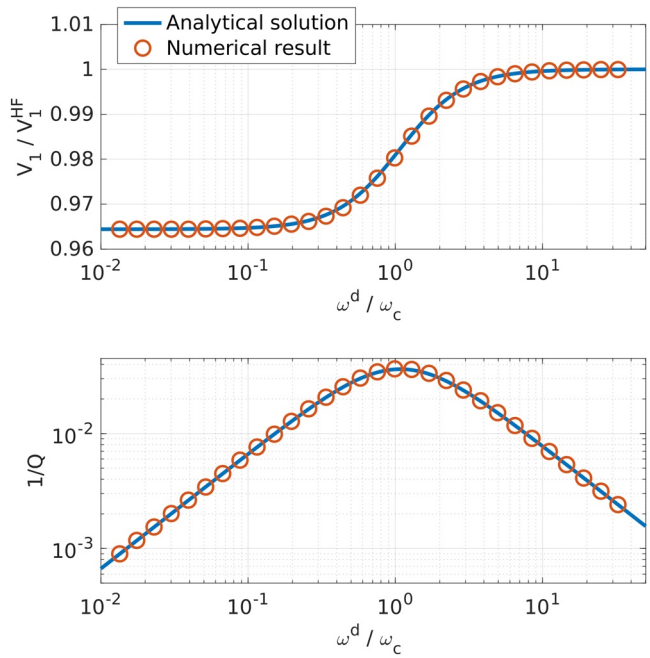

Figure 15. A comparison between numerically calculated dimensional phase velocities (up) and $1/Q$ (down) against an analytical solution of Biot's equations. Each red circle corresponds to a numerical simulation. The phase velocity V_1 is normalized by the velocity in the high frequency limit V_1^{HF} and the dimensional angular frequency ω^d is normalized against Biot's frequency ω_c. The material parameters are those from Table 3.

ond-order. Therefore, the scheme with $\chi = 1/2$ is used for the numerical solution of Biot's equations in the rest of the manuscript.

6. Numerical Experiments

We here present a series of simulations based on Biot's equations in two and three dimensions. We discuss some basic aspects of poroelasticity, namely, wave propagation in homogeneous poroacoustic and poroelastic media, in isotropic and anisotropic poroelastic media, and at low- and high-frequency regimes.

6.1. Wave Propagation in 2D Poroelastic Media

6.1.1. PoroAcoustic and PoroElastic Media

We examine the difference between poroelastic and poroacoustic wave propagation at low- and high-frequencies in two dimensions. The material properties are those of an isotropic sandstone (Table 4). For the poroacoustic material, we set the shear modulus c_{55} to zero. A 2D square domain of 9.35×9.35 m is used. We define 32 threads per blocks in x- and z-directions with 128 blocks in x- and z-directions, which result in $4{,}095 \times 4{,}095$ grid resolution having $\approx 16 \times 10^6$ grid cells. We apply a Gaussian distribution (55) with $l_x = 0.08$, $l_y = 0.08$, and $A_0 = 1$ at the center of the model domain to the solid velocity (V_z) as an initial condition for the poroacoustic and low frequency poroelastic simulations. For the high frequency poroelastic simulations we also apply the Gaussian distribution to the fluid pressure p_f.

Figure 17 shows the total pressure ($\overline{p}$) and solid velocity (V_x) fields for poroacoustic and poroelastic simulations. In total, 5,000 time steps were performed and the total physical simulation time was approximately $t = 9 \times 10^{-4}$ s. The simulations were performed on a single Tesla V100 PCIe GPU. The running time was approximately 55 s for each simulation. For a performance comparison, a few simulations were executed on a single Tesla V100 Nvlink GPU, and the running time was approximately 51 s. Note, that the 2D codes performance is not optimized as it is done for 3D codes. For optimized 2D codes, the performance might be much higher. In the poroacoustic simulations (Figures 17a and 17b), the initial condition corresponds to the low frequency regime and

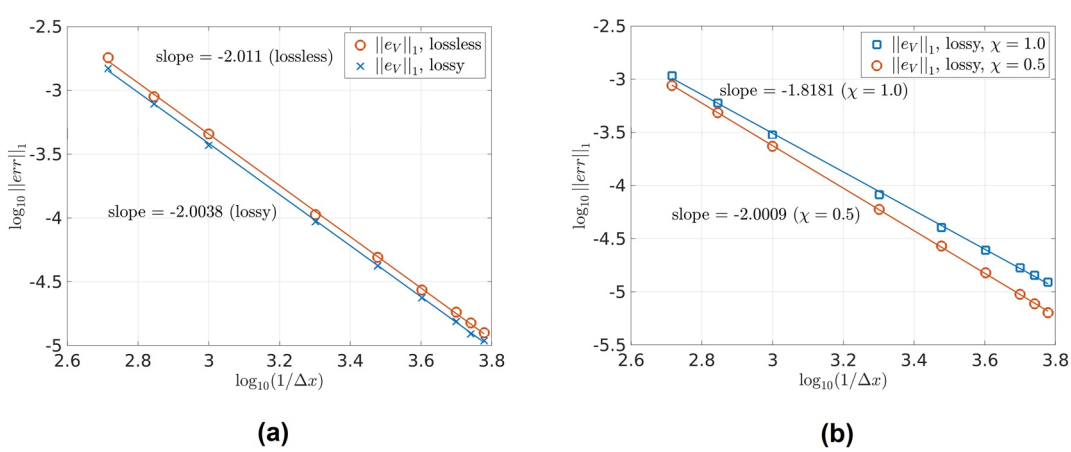

Figure 16. The truncation error magnitudes of the numerically estimated velocities. (a) The low frequency source and (b) f_c of the source is close to the frequency of $1/Q_1$ maximum. The material parameters are those from Table 3.

Table 4
Properties of Anisotropic Poroelastic Rocks Used for Numerical Simulations

Sandstone (VTI)			Glass-epoxy (VTI)	Sandstone (isotropic)
Rock properties				
K_s	(GPa)	80	40	40
ρ_s	(kg/m^3)	2,500	1,815	2,500
c_{11}	(GPa)	71.8	39.4	36
c_{12}	(GPa)	3.2	1.2	12
c_{13}	(GPa)	1.2	1.2	12
c_{33}	(GPa)	53.4	13.1	36
c_{55}	(GPa)	26.1	3.0	12
ϕ	(−)	0.2	0.2	0.2
k_1	(m^2)	600×10^{-15}	600×10^{-15}	600×10^{-15}
k_3	(m^2)	100×10^{-15}	100×10^{-15}	600×10^{-15}
T_1	(−)	2	2	2
T_3	(−)	3.6	3.6	3.6
K_f	(GPa)	2.5	2.5	2.5
ρ_f	(kg/m^3)	1,040	1,040	1,040
η	(kg/m·s)	10^{-3}	10^{-3}	10^{-3}

VTI corresponds to a vertical transverse isotropic medium.

only the fast (longitudinal) wave V_1 can be observed. Also note that the 2D poroacoustic medium cannot unload the initial condition applied to the solid velocity field, which is represented by non-zero amplitudes at the center of the model (Figure 17b). In the poroelastic simulations (Figures 17c and 17d), the initial condition corresponds to the low frequency regime and only two waves can be observed—the fast (longitudinal) wave V_1 and the shear wave V_s. In the poroelastic simulations (Figures 17e and 17f), the initial condition of a Gaussian shape with $l_x = 8 \times 10^{-4}$ and $l_y = 8 \times 10^{-4}$ corresponds to the high frequency regime. Three waves can be clearly observed—the fast (longitudinal) wave V_1, the shear wave V_s and the slow (longitudinal) wave V_2 (Figures 17e and 17f).

6.1.2. Anisotropic Poroelastic Media

In this section, we reproduce similar two dimensional results shown in de la Puente et al. (2008); Lemoine et al. (2013), so the present simulations can be qualitatively compared to the previous works. The material properties of anisotropic rocks are similar to those of de la Puente et al. (2008); Lemoine et al. (2013) (Table 4). We apply a Gaussian distribution to σ_{zz} and p_f with $l_x = 0.08$, $l_y = 0.08$, and $A_0 = 1$ to the center of the numerical model. Other parameters are the same as in the previous 2D simulations. The simulations were performed on a single Tesla V100 Nvlink GPU. The running time was approximately 51 s for both (glass-epoxy and sandstone-VTI) models, 5,000 time steps were performed. The total physical simulation time was $t = 6.15 \times 10{-}04$ seconds for the anisotropic sandstone and $t = 7.061 \times 10{-}04$ seconds for the glass-epoxy model. The results of the solid velocity fields V_x and V_z are shown in Figures 18 and 19. In analogy to de la Puente et al. (2008); Lemoine et al. (2013), we show numerical results for inviscid models ($\eta = 0$) and viscid models ($\eta \neq 0$). Simulations in inviscid media mimic the high frequency regime, therefore, fast, quasi-shear, and slow waves can be observed (Figures 18a and 18b and Figures 19a and 19b). Simulations in viscid media correspond to the low frequency regime, therefore, only fast and quasi-shear waves are observed (Figures 18c and 18d and Figures 19c and 19d).

6.2. Wave Propagation in 3D Anisotropic Poroelastic Media

We simulate a wave propagating in 3D for the anisotropic poroelastic material whose properties are of the glass-epoxy (Table 4), the properties in the x-direction are duplicated to the y-direction. The simulations were performed on eight Tesla V100 Nvlink GPUs. A three dimensional cubic domain of 9.35 m × 9.35 m × 9.35 m is used. The total resolution is 1,022 × 1,022 × 1,022 grid cells in x-, y-, and z-dimensions, respectively, which results in $\approx 1 \times 10^9$ grid cells. We apply a Gaussian distribution to the fluid pressure p_f (fluid injection) with $l_x = 0.18$, $l_y = 0.18$, $l_z = 0.18$ and $A_0 = 10^{10}$ at the center of the numerical model. The running time was approximately 73 s for all simulations, 1,050 time steps were performed. The total physical simulation time was 6.8×10^{-4} seconds. This model configuration corresponds to the low frequency regime.

Figure 20 shows the solid velocity field $V = V_x + V_y + V_z$. The velocity field is projected into several slices, also the isosurfaces of the wave amplitudes of $\pm 3 \times 10^{-3}$ are shown. Figure 21a shows the solid velocity field V_x for the same model (Figure 20) while Figure 21b shows V_x of the 100 times smaller model (the size is 0.0935^3 m), which corresponds to the high frequency regime. The initial condition was scaled accordingly, $l_x = 0.018$, $l_y = 0.018$, and $l_z = 0.018$ (A_0 is the same) and the total physical simulation time was also scaled to 6.8×10^{-6} seconds. The behavior of fast and quasi-shear waves is similar in Figures 21a and 21b but the slow P-wave behavior is different. In Figure 21a, the slow P-wave degenerated into a diffusion mode representing viscous fluid flow in porous media while in Figure 21b the slow P-wave behaves as a true propagating wave.

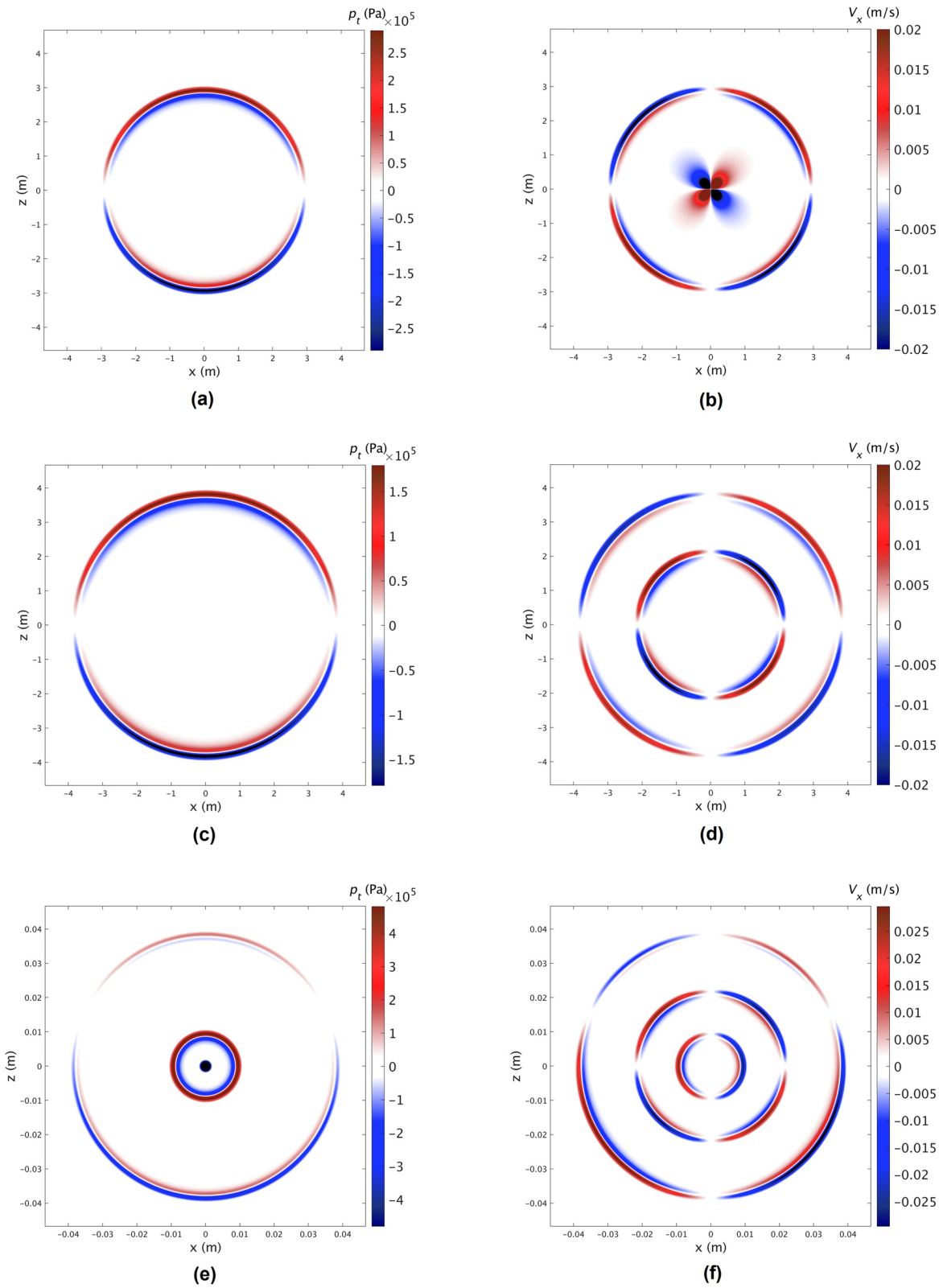

Figure 17. Numerical simulation of a propagating waves. (a), (c), (e) show the total pressure field $\overline{p}$; (v), (d), (f) show the velocity field Vx. Plots (a) and (b) correspond to the poroacoustic medium, (c) and (d) correspond to the poroelastic medium (low frequency regime), and (e) and (f) correspond to the poroelastic medium (high frequency regime). The total physical simulation time is approximately $t = 9 \times 10^{-4}$ seconds. The material properties are those of an isotropic sandstone (Table 4).

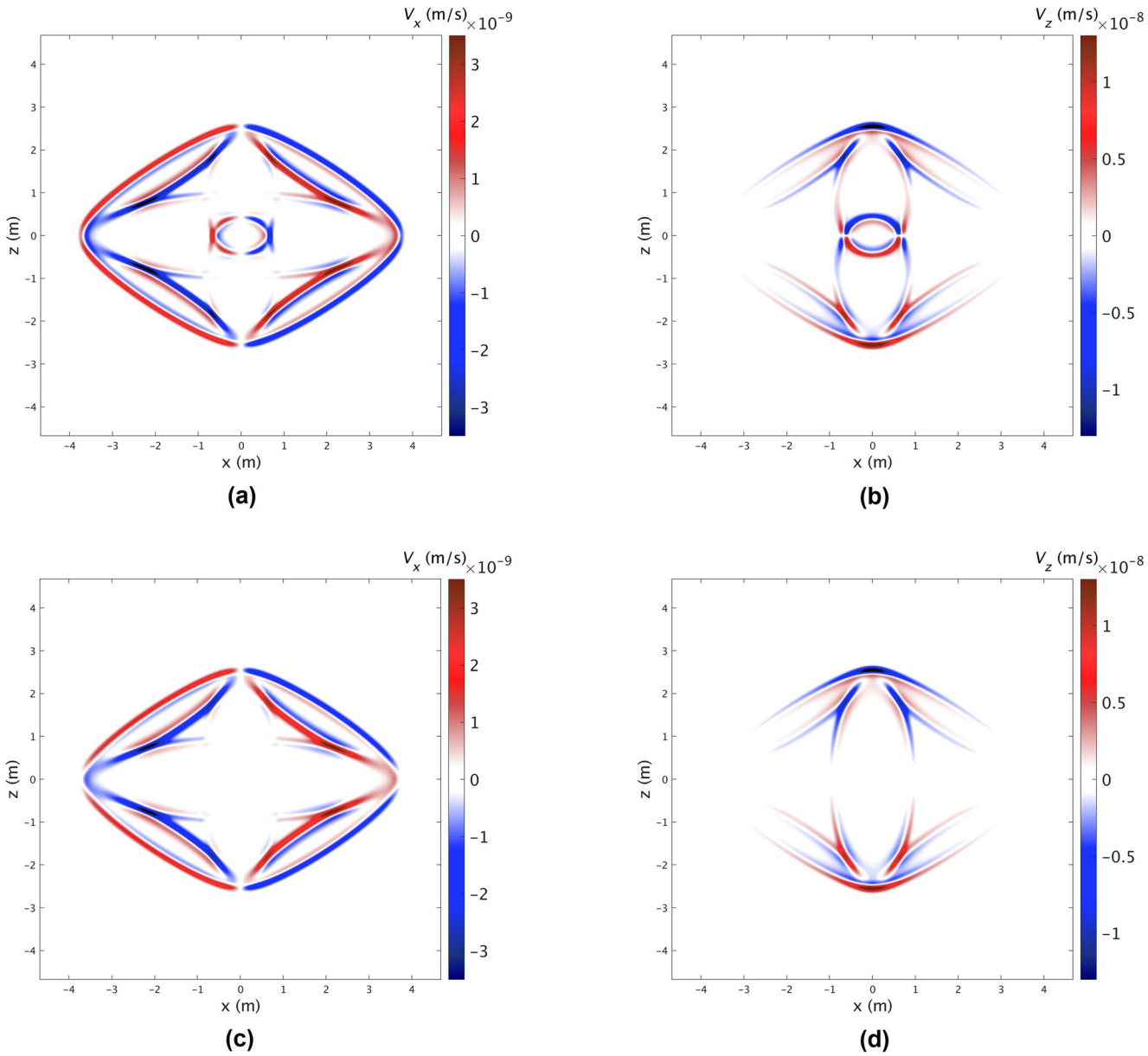

Figure 18. Snapshots showing velocity fields V_x and V_z in the epoxy-glass medium (Table 4). Panels (a) and (b) correspond to the inviscid medium ($\eta = 0$), panels (c) and (d) correspond to the viscid medium ($\eta \neq 0$). The total physical simulation time is $t = 7.061 \times 10^{-04}$ seconds.

7. Conclusions

We developed a multi-GPU solver for the anisotropic elastodynamic Biot's equations in 1D, 2D, and 3D using the CUDA C programming language leveraging the parallel processing power of GPUs. We implement a simple approach to circumvent the stiffness of Biot's equations by using an implicit scheme for Darcy's flux while keeping explicit updates in the iteration loop. We achieve a close-to-ideal parallel efficiency (98% and 96%) on weak scaling tests up to 128 GPUs by overlapping MPI communication and computations. We also achieve an effective memory throughput of 90% of the memory copy throughput. Our multi-GPU implementation of Biot's equations permits to tackle high spatial resolution and exhibits fast execution times. We perform 1,000 explicit time steps in 95 s for a model involving 1.5 billion grid cells (1152^3) on 8 Tesla

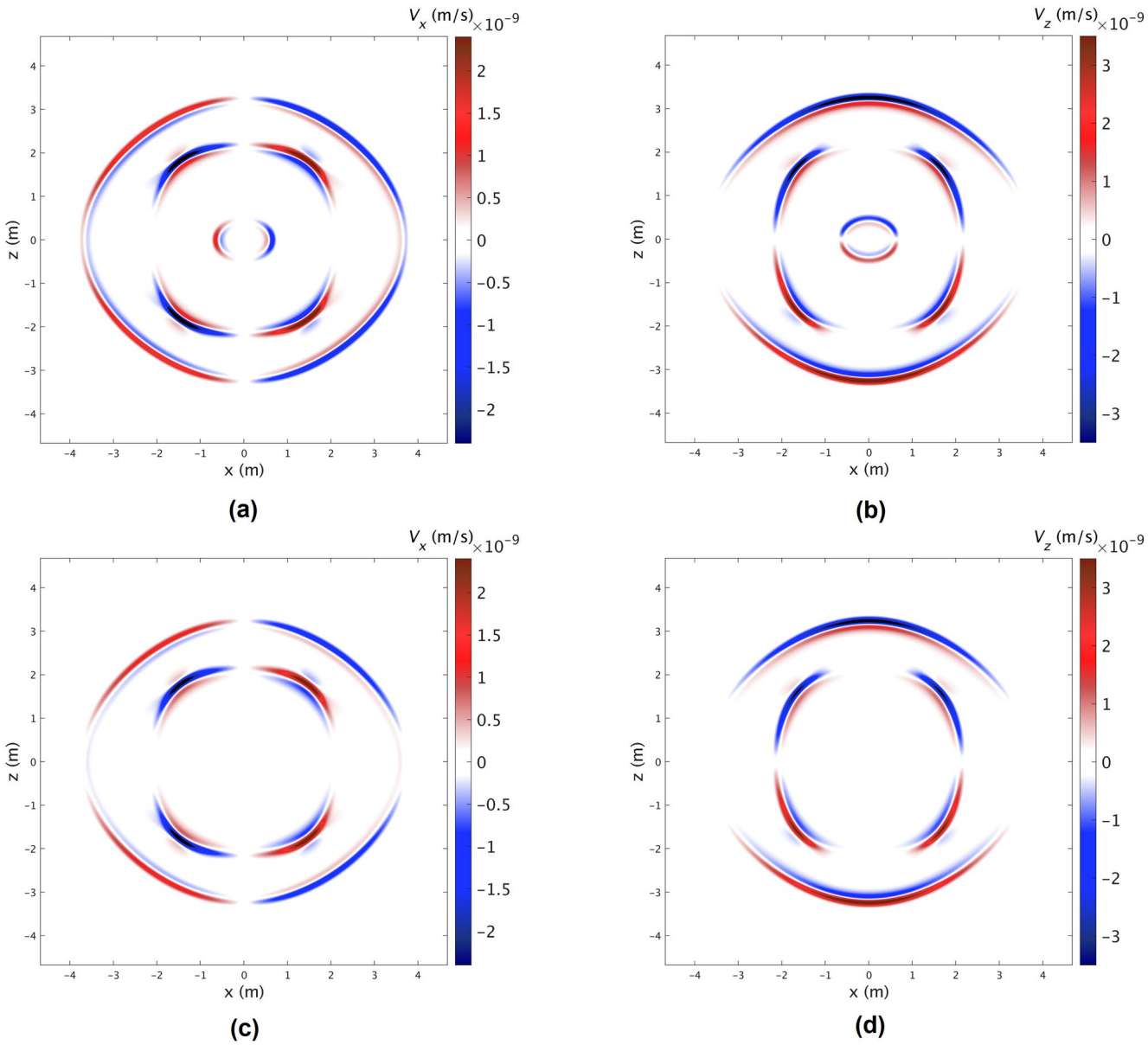

Figure 19. Snapshots showing velocity fields V_x and V_z in the sandstone-VTI medium (Table 4). Panels (a) and (b) correspond to the inviscid medium ($\eta = 0$), panels (c) and (d) correspond to the viscid medium ($\eta \neq 0$). The total physical simulation time is $t = 6.15 \times 10{-}04$ seconds. VTI, vertical transverse isotropic medium.

V100 32 GB Nvlink GPUs using double-precision arithmetics. We analyze the stability and accuracy of the three different numerical schemes and suggest the best out of three. We benchmark the numerical solver against an analytical solution of Biot's equations and present a comprehensive dimensional analysis of Biot's equations to reduce the number of material parameters from ten to four. Our numerical application to resolve Biot's equations enables practical applications in geophysics, engineering, biophysics, and the further understanding the underlying hydromechanically coupled processes in 3D.

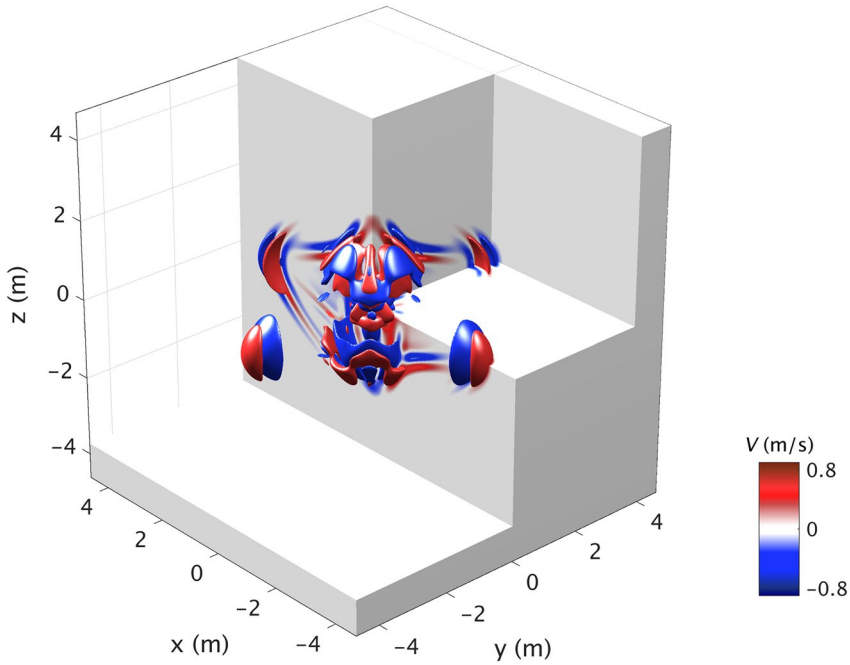

Figure 20. Snapshots showing the total solid velocity field $V = V_x + V_y + V_z$ in the medium having the properties of the glass-epoxy (Table 4). The velocity field is projected into X–Z and Y–Z slices. Red and blue isosurfaces denote the wave amplitudes of ±0.4. The anisotropic nature of the model is clearly visible due to the non-symmetric velocity field pattern. The total physical simulation time is 6.8×10^{-4} s.

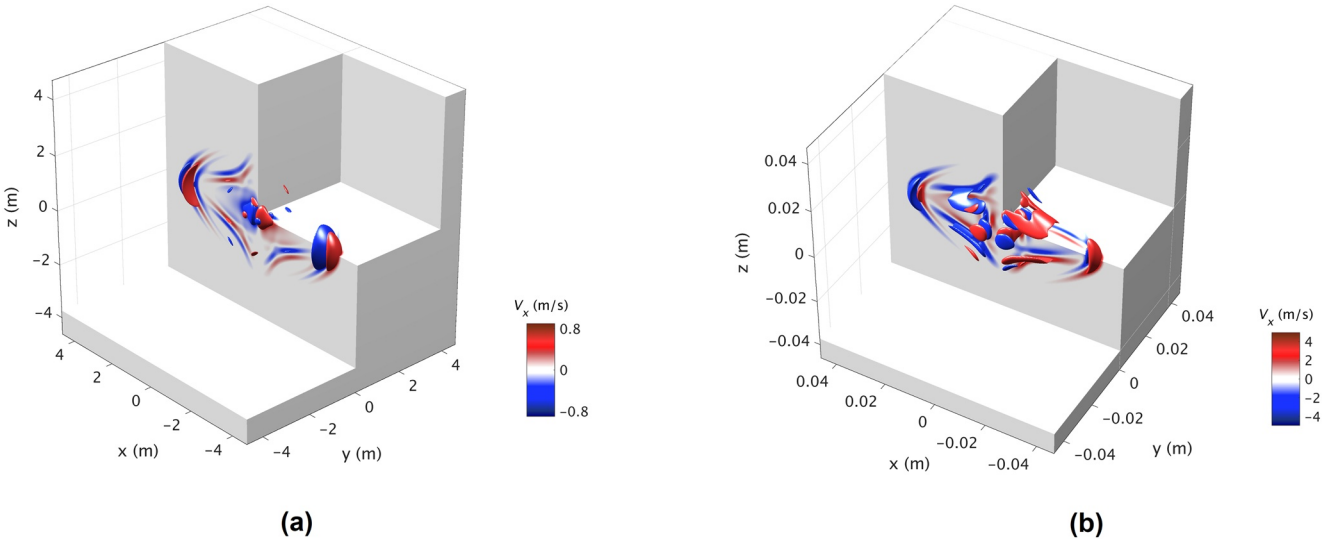

Figure 21. Snapshots showing the solid velocity field V_x in the medium having the properties of the glass-epoxy (Table 4). Panel (a) shows V_x of the same model as in Figure 20, red and blue isosurfaces denote the wave amplitudes of ±0.4, the total physical simulation time is 6.8×10^{-4} seconds. Panel (b) shows V_x of the 100 times smaller model, which corresponds to the high frequency regime, the total physical simulation time is 6.8×10^{-6} seconds. Red and blue isosurfaces denote the wave amplitudes of ±3.0.

Appendix A: Equations Describing A Single Phase Continuum Material

A1. Stress-Strain Relations

For a single phase linear elastic continuum material, the stress-strain relation (Hooke's Law) is

$$\boldsymbol{\sigma} = \mathbf{C} : \boldsymbol{\epsilon} \tag{A1}$$

or using index (Einstein) notation

$$\sigma_{ij} = \mathbf{C}_{ijkl}\, \epsilon_{kl}, \tag{A2}$$

where $\boldsymbol{\sigma}$ is the second rank stress tensor, ϵ is the second rank strain tensor, $\mathbf{C}$ is the fourth rank stiffness tensor, : denotes the double dot product and $i, j, k, l = \overline{1,\ldots,3}$. Bold symbols denote tensors and italic (non-bold) symbols denote tensor components. For small deformations, the strain tensor is defined as

$$\epsilon = \frac{1}{2}\left(\nabla \otimes \boldsymbol{u} + \left(\nabla \otimes \boldsymbol{u}\right)^{\mathrm{T}}\right) \tag{A3}$$

or

$$\epsilon_{kl} = \frac{1}{2}\left(\nabla_l u_k + \nabla_k u_l\right), \tag{A4}$$

where $\boldsymbol{u}$ is the displacement, $\otimes$ denotes the tensor product, ∇ denotes the nabla operator, and the superscript T corresponds to the transpose operator. For larger strains, an incremental formulation is preferable. Therefore, the relation between displacements and the time derivative of strain is

$$\frac{\partial \sigma_{ij}}{\partial t} = c_{ijkl}\frac{1}{2}\left(\nabla_l v_k^s + \nabla_k v_l^s\right), \tag{A5}$$

where the velocity is defined as $v_i^s = \partial u_i \,/\, \partial t$. Note, that in the case of small linear deformations, the definition (A1)–(A4) coincides with the definition (A5). For large deformations the definition (A1)–(A4) is not longer valid due to the absence of second-order terms of the finite strain tensor while the definition (A5) still holds. In this article, we only use the incremental formulation (A5). In isotropic media, the stress and strain tensors can be separated into volumetric and deviatoric parts. Equation (A5) can be rewritten as

$$\frac{\partial \sigma_{ij}}{\partial t} = K\nabla_k v_k \delta_{ij} + 2G\left(\frac{1}{2}\left(\nabla_j v_i + \nabla_i v_j\right) - \frac{1}{3}\nabla_k v_k \delta_{ij}\right). \tag{A6}$$

Equation (A6) can be simplified, once pressure and deviatoric stresses are introduced,

$$\frac{\partial \sigma_{ij}}{\partial t} = -\frac{\partial p}{\partial t}\delta_{ij} + \frac{\partial \tau_{ij}}{\partial t}, \tag{A7}$$

where pressure p is

$$\frac{\partial p}{\partial t} = -K\nabla_k v_k \tag{A8}$$

and the deviatoric stress tensor τ_{ij} is expressed as

$$\frac{\partial \tau_{ij}}{\partial t} = 2G\left(\frac{1}{2}\left(\nabla_j v_i + \nabla_i v_j\right) - \frac{1}{3}\nabla_k v_k \delta_{ij}\right). \tag{A9}$$

A2. Dynamic Equations

The conservation of linear momentum for a single phase material is

$$\rho \frac{\partial v_i}{\partial t} = \nabla_j \sigma_{ij}. \tag{A10}$$

Equation (A10) can also be called equation of motion or elastodynamic force balance law. By separating the stress tensor into deviatoric and volumetric parts, Equation (A10) can be written as

$$\rho \frac{\partial v_i}{\partial t} = \nabla_j (-p\delta_{ij} + \tau_{ij}) \tag{A11}$$

In summary, the constitutive Equations (A8) and (A9) and the conservation of linear momentum (A11) fully describe the behavior of a single phase material. Depending on the initial conditions (or the source terms) and the material parameters, the response of a single phase material may include one fast (longitudinal) wave and one shear wave.

Appendix B: Poroelastic Parameters

Three experiments permit to determine the poroelastic parameters required for Biot's equations (Makhnenko & Podladchikov, 2018). The drained bulk modulus K_d can be measured under drained experiments. In such experiments the pore fluid is allowed to leave the rock during loading and that pore fluid pressure is maintained at a constant level (p_f = const, see Equation (1))

$$K_d = \frac{1}{\nabla_k v_k^s} \frac{\partial \overline{p}}{\partial t}\bigg|_{(p_f = \text{const})} \tag{B1}$$

The undrained bulk modulus K_u can be obtained under undrained experiments. In such experiments the fluid content inside the rock does not change during loading, meaning that fluid does not flow through the boundaries of the considered element ($\nabla_k q_k^D = 0$, see Equation (1))

$$K_u = \frac{1}{\nabla_k v_k^s} \frac{\partial \overline{p}}{\partial t}\bigg|_{(\nabla_k q_k^D = 0)} \tag{B2}$$

The Biot-Willis parameter α can be obtained under unjacketed experiments, in which an increase in the total pressure $\overline{p}$ is equal to the increase in fluid pressure p_f: ($d\overline{p} = dp_f$, see Equation (1)). For more information about how to measure poroelastic constants in rock samples, we refer to R. W. Zimmerman (1990).

Appendix C: An Alternative Dimensional Analysis of Biot's Equations

In (12), instead of the base quantity ρ_t, an alternative choice is possible, namely, ρ_a. In this case, Equation (12) reads

$$\rho_a \begin{pmatrix} \frac{\rho_t}{\rho_a} & -\frac{\rho_f}{\rho_a} \\ -\frac{\rho_a}{\rho_t} & 1 \end{pmatrix} \begin{pmatrix} \frac{\partial v^s}{\partial t} \\ -\frac{\partial q^D}{\partial t} \end{pmatrix} = \begin{pmatrix} \frac{\partial \overline{\sigma}}{\partial x} \\ \frac{\eta}{k} q^D + \frac{\partial p_f}{\partial x} \end{pmatrix}, \tag{C1}$$

where

$$\alpha_a = \frac{\alpha}{B}\left(1 + \frac{4/3G}{K_u}\right). \tag{C2}$$

In the resulting system, Equation (17) is still the same, while Equation (18) becomes

$$\left(I_1\right)^2 \begin{pmatrix} \rho_{ta} & -\rho_{fa} \\ -\rho_{fa} & 1 \end{pmatrix} \begin{pmatrix} \dfrac{\partial \tilde{v}^s}{\partial \tilde{t}} \\ -\dfrac{\partial \tilde{q}^D}{\partial \tilde{t}} \end{pmatrix} = \begin{pmatrix} \dfrac{\partial \tilde{\bar{\sigma}}}{\partial \tilde{x}} \\ I_2 \tilde{q}^D + \dfrac{\partial \tilde{p}_f}{\partial \tilde{x}} \end{pmatrix}, \tag{C3}$$

where $\rho_{fa} \equiv \rho_f / \rho_a$, $\rho_{ta} \equiv \rho_t / \rho_a$,

$$I_1 = \sqrt{\rho_a s_{11}^d}\, \frac{L_x^*}{\tau^*}, \tag{C4}$$

and

$$I_2 = \frac{\eta s_{11}^d}{k} \frac{(L_x^*)^2}{\tau^*} \equiv \frac{1}{D} \frac{(L_x^*)^2}{\tau^*}, \tag{C5}$$

$$D = \frac{k}{\eta s_{11}^d}. \tag{C6}$$

The alternative four dimensionless parameters α, α_a, ρ_{fa} and ρ_{ta} now define the coupling between the solid and fluid phases. If we similarly set $I_1 = 1$, then $L_x^* = \tau^* / \sqrt{\rho_a s_{11}^d}$ and I_2 becomes

$$I_2 = \frac{\eta}{k \rho_a} \tau^*. \tag{C7}$$

Thus, we choose the new τ^* as

$$\tau^* = \left(\frac{\eta}{k \rho_a}\right)^{-1} \equiv \left(\frac{\eta \phi}{k \rho_f T}\right)^{-1}, \tag{C8}$$

We end up with $I_2 = 1$ and the transformation frequency now is equivalent to the Biot's characteristic frequency (40). Indeed, the dimensional angular frequency ω^d is calculated as $\omega^d = \omega \omega^*$, where ω is the non-dimensional angular frequency and ω^* is the transformation frequency (analogous to (39))

$$\omega^* = \frac{1}{\tau^*} \equiv \frac{\eta \phi}{k \rho_f T}, \tag{C9}$$

which is exactly the Biot's characteristic frequency ω_c (40). This is the main advantage of the new dimensional analysis. The disadvantage is that the drained wave velocity V_d formula disappears in (C4), which makes the interpretation of I_1 in terms of usual physical quantities less transparent. By using this new dimensional analysis, Figures 1–4 will remain almost the same with the only slight shift of the transition frequency closer to $\omega = 1$. This shift in ω is defined by the ratio between ρ_t and $(\rho_f T / \phi)$.

Appendix D: Elastodynamic Biot's Equations For Anisotropic Media

D1. Arbitrary Anisotropic Media

Elastodynamic Biot's equations in arbitrary anisotropic media can be written in the first order form. The stress-strain relations are

$$\frac{\partial \bar{\sigma}_{ij}}{\partial t} = c_{ijkl}^u \nabla_k v_l^s + \alpha_{ij} M \nabla_k q_k^D, \tag{D1}$$

$$\frac{\partial p_f}{\partial t} = -M\left(\alpha_{ij}\nabla_i v_j^s + \nabla_m q_m^D\right), \tag{D2}$$

where c_{ijkl}^u is the 4th order undrained stiffness tensor and α_{ij} is the Biot-Willis parameter represented by a second order tensor. The conservation of linear momentum reads

$$\frac{\partial v_i^s}{\partial t} = \varrho_{11}\nabla_i\bar{\sigma}_{ij} + \varrho_{12}\left(\nabla_i p_f + \frac{\eta}{k_i}q_i^D\right), \tag{D3}$$

$$\frac{\partial q_i^D}{\partial t} = -\varrho_{21}\nabla_i\bar{\sigma}_{ij} - \varrho_{22}\left(\nabla_i p_f + \frac{\eta}{k_i}q_i^D\right), \tag{D4}$$

where

$$\varrho_{ij} = \begin{pmatrix} \varrho_{11} & \varrho_{12} \\ \varrho_{21} & \varrho_{22} \end{pmatrix} = \frac{1}{\Theta}\begin{pmatrix} \rho_a & \rho_f \\ \rho_f & \rho_t \end{pmatrix}, \tag{D5}$$

$\Theta = \rho_t\rho_a - \rho_f^2$ and k_i denotes permeability in $i-$ direction, respectively. In (D1)–(D5), ∂_t represents a time derivative, v_i and q_i^D are vector fields, σ_{ij} is a tensor field, p_f is a scalar field. All the material parameters, namely, c_{ijkl}^u, α_{ij}, M, ϱ_{ij}, η, k_i are constant in time but may vary in space.

D2. Orthorhombic Media

An orthorhombic medium is described by nine elastic components of the stiffness tensor. We use the shortened Voigt notation as a shortcut. The stress-strain relations are

$$\frac{\partial\bar{\sigma}_{xx}}{\partial t} = c_{11}^u\partial_x v_x^s + c_{12}^u\partial_y v_y^s + c_{13}^u\partial_z v_z^s + \alpha_1 M\left(\partial_x q_x^D + \partial_y q_y^D + \partial_z q_z^D\right), \tag{D6}$$

$$\frac{\partial\bar{\sigma}_{yy}}{\partial t} = c_{12}^u\partial_x v_x^s + c_{22}^u\partial_y v_y^s + c_{23}^u\partial_z v_z^s + \alpha_2 M\left(\partial_x q_x^D + \partial_y q_y^D + \partial_z q_z^D\right), \tag{D7}$$

$$\frac{\partial\bar{\sigma}_{zz}}{\partial t} = c_{13}^u\partial_x v_x^s + c_{23}^u\partial_y v_y^s + c_{33}^u\partial_z v_z^s + \alpha_3 M\left(\partial_x q_x^D + \partial_y q_y^D + \partial_z q_z^D\right), \tag{D8}$$

$$\frac{\partial\bar{\sigma}_{yz}}{\partial t} = c_{44}^u\left(\partial_z v_y^s + \partial_y v_z^s\right), \tag{D9}$$

$$\frac{\partial\bar{\sigma}_{xz}}{\partial t} = c_{55}^u\left(\partial_z v_x^s + \partial_x v_z^s\right), \tag{D10}$$

$$\frac{\partial\bar{\sigma}_{xy}}{\partial t} = c_{66}^u\left(\partial_y v_x^s + \partial_x v_y^s\right), \tag{D11}$$

$$\frac{\partial p_f}{\partial t} = -\alpha_1 M\partial_x v_x^s - \alpha_2 M\partial_y v_y^s - \alpha_3 M\partial_z v_z^s - M\left(\partial_x q_x^D + \partial_y q_y^D + \partial_z q_z^D\right), \tag{D12}$$

∂_i represents a spatial derivative in $i-$ direction. The relation between the drained stiffness matrix c_{ij} and the undrained stiffness matrix c_{ij}^u is

$$c_{ij}^u = c_{ij} + \alpha_i\alpha_j M, \tag{D13}$$

where $\alpha_i = (\alpha_1, \alpha_2, \alpha_3, 0, 0, 0)$ and $\alpha_j = (\alpha_1, \alpha_2, \alpha_3, 0, 0, 0)^{\mathrm{T}}$ are the Biot-Willis coefficients,

$$\alpha_i = 1 - \left(\sum_{j=1}^{3} c_{ij} \right) / (3K_g), \tag{D14}$$

for $i = 1, 2, 3$. For example,

$$\alpha_1 = 1 - \frac{c_{11} + c_{12} + c_{13}}{3K_g}, \tag{D15}$$

$$\alpha_2 = 1 - \frac{c_{21} + c_{22} + c_{23}}{3K_g}, \tag{D16}$$

$$\alpha_3 = 1 - \frac{c_{13} + c_{23} + c_{33}}{3K_g} \tag{D17}$$

and M is the solid-fluid coupling modulus, defined as

$$M = \left(\phi / K_f + (1 - \phi) / K_g - K^* / K_g^2 \right)^{-1}, \tag{D18}$$

$$K^* = \frac{1}{9} \sum_{i=1}^{3} \sum_{j=1}^{3} c_{ij} = \left[c_{11} + c_{22} + c_{33} + 2(c_{12} + c_{13} + c_{23}) \right] / 9 \tag{D19}$$

The modulus K^* is usually called the generalized bulk modulus, which, in fact, represents the Voigt average of the bulk modulus for an orthorhombic symmetry system. The conservation of linear momentum reads

$$\frac{\partial q_x^D}{\partial t} = \varrho_{21} \left(-\partial_x \bar{\sigma}_{xx} - \partial_y \bar{\sigma}_{xy} - \partial_z \bar{\sigma}_{xz} \right) - \varrho_{22} \left(\partial_x p_f + \frac{\eta}{k_1} q_x \right), \tag{D20}$$

$$\frac{\partial q_y^D}{\partial t} = \varrho_{21} \left(-\partial_x \bar{\sigma}_{xy} - \partial_y \bar{\sigma}_{yy} - \partial_z \bar{\sigma}_{yz} \right) - \varrho_{22} \left(\partial_y p_f + \frac{\eta}{k_2} q_y \right), \tag{D21}$$

$$\frac{\partial q_z^D}{\partial t} = \varrho_{21} \left(-\partial_x \bar{\sigma}_{xz} - \partial_y \bar{\sigma}_{yz} - \partial_z \bar{\sigma}_{zz} \right) - \varrho_{22} \left(\partial_z p_f + \frac{\eta}{k_3} q_z \right), \tag{D22}$$

$$\frac{\partial v_x^s}{\partial t} = \varrho_{11} \left(\partial_x \bar{\sigma}_{xx} + \partial_y \sigma_{xy} + \partial_z \bar{\sigma}_{xz} \right) + \varrho_{12} \left(\partial_x p_f + \frac{\eta}{k_1} q_x \right), \tag{D23}$$

$$\frac{\partial v_y^s}{\partial t} = \varrho_{11} \left(\partial_x \bar{\sigma}_{xy} + \partial_y \bar{\sigma}_{yy} + \partial_z \bar{\sigma}_{yz} \right) + \varrho_{12} \left(\partial_y p_f + \frac{\eta}{k_2} q_y \right), \tag{D24}$$

$$\frac{\partial v_z^s}{\partial t} = \varrho_{11} \left(\partial_x \bar{\sigma}_{xz} + \partial_y \bar{\sigma}_{yz} + \partial_z \bar{\sigma}_{zz} \right) + \varrho_{12} \left(\partial_z p_f + \frac{\eta}{k_3} q_z \right), \tag{D25}$$

where ϱ_{ij} is given by (D5).

Appendix E: Discretization of Biot's Equations

For a given function $g^n_{i,j,k} = g(t^l, x_i, y_j, z_k)$, the following operators for the time evolution are introduced

$$D^1_t[g] = \frac{\partial g}{\partial t} = \frac{g^{l+1/2}_{i,j,k} - g^{l-1/2}_{i,j,k}}{\Delta t}, \tag{E1}$$

$$D^2_t[g] = \frac{\partial g}{\partial t} = \frac{g^{l+1}_{i+1/2,j,k} - g^{l}_{i+1/2,j,k}}{\Delta t}, \tag{E2}$$

$$\bar{D}_\chi[g] = \chi g^{l+1}_{i+1/2,j,k} + (1-\chi) g^{l}_{i+1/2,j,k}, \tag{E3}$$

where $\chi \in [0;1]$ is the weight parameter. The following operators for the spatial derivatives are introduced

$$D^1_x[g] = \frac{\partial g}{\partial x} = \frac{g^{l+1/2}_{i+1,j,k} - g^{l+1/2}_{i,j,k}}{\Delta x},\ D^1_y[g] = \frac{\partial g}{\partial y} = \frac{g^{l+1/2}_{i,j+1,k} - g^{l+1/2}_{i,j,k}}{\Delta y},\ D^1_z[g] = \frac{\partial g}{\partial z} = \frac{g^{l+1/2}_{i,j,k+1} - g^{l+1/2}_{i,j,k}}{\Delta z}, \tag{E4}$$

$$D^2_x[g] = \frac{\partial g}{\partial x} = \frac{g^{l}_{i+1/2,j,k} - g^{l}_{i-1/2,j,k}}{\Delta x},\ D^2_y[g] = \frac{\partial g}{\partial y} = \frac{g^{l}_{i,j+1/2,k} - g^{l}_{i,j-1/2,k}}{\Delta y},$$
$$D^2_z[g] = \frac{\partial g}{\partial z} = \frac{g^{l}_{i,j,k+1/2} - g^{l}_{i,j,k-1/2}}{\Delta z}, \tag{E5}$$

The following averaging operators for the material parameters are introduced

$$([g]_1)_{i+1/2,j,k} = \left(g_{i,j,k} + g_{i+1,j,k}\right)/2, \tag{E6}$$

$$([g]_2)_{i+1/2,j+1/2,k} = 4\left(1/g_{i,j,k} + 1/g_{i+1,j,k} + 1/g_{i,j+1,k} + 1/g_{i+1,j+1,k}\right)^{-1}. \tag{E7}$$

For simplicity, equations only in x- direction are shown in the discrete form. A few additional operators are introduced

$$\nabla \cdot v^s = D^2_x[v^s_x] + D^2_y[v^s_y] + D^2_z[v^s_z], \nabla \cdot q^D = D^2_x[q^D_x] + D^2_y[q^D_y] + D^2_z[q^D_z]. \tag{E8}$$

The discretized system of equations is

$$D^1_t[\bar{p}] = -K_u \nabla \cdot v^s - K_u B \nabla \cdot q^D, \tag{E9}$$

$$D^1_t[p_f] = -K_u B \nabla \cdot v^s - K_u B / \alpha \nabla \cdot q^D, \tag{E10}$$

$$D^1_t[\bar{\tau}_{xx}] = 2G\left(D^2_x[v^s_x] - 1/3\nabla \cdot v^s\right), \tag{E11}$$

Discretization of $\bar{\tau}_{yy}$ and $\bar{\tau}_{zz}$ is in analogy to that of $\bar{\tau}_{xx}$. The stress deviator tensor field is discretized as

$$D^1_t[\bar{\tau}_{xy}]_{i+1/2,j+1/2,k} = [G]_2\left(D^2_x[v^s_y] + D^2_y[v^s_x]\right), \tag{E12}$$

Discretization of $\bar{\tau}_{xz}$ and $\bar{\tau}_{yz}$ is in analogy to that of $\bar{\tau}_{xy}$. The total stress tensor field $\nabla \cdot \bar{\sigma}_{xx}$ is

$$\nabla \cdot \bar{\sigma}_{xx} = D^1_x[\bar{\tau}_{xx}] - D^1_x[\bar{p}] + \frac{[\bar{\tau}_{xy}]^{l+1/2}_{i+1/2,j+1/2,k} - [\bar{\tau}_{xy}]^{l+1/2}_{i+1/2,j-1/2,k}}{\Delta y} + \frac{[\bar{\tau}_{xz}]^{l+1/2}_{i+1/2,j,k+1/2} - [\bar{\tau}_{xz}]^{l+1/2}_{i+1/2,j,k-1/2}}{\Delta z}. \tag{E13}$$

The Darcy's flux and the velocity vector fields in the discrete form are

$$D_t^2[q_x^D] = \frac{1}{[\Theta]_1}\left(-[\rho_f]_1 \nabla \cdot \bar{\sigma}_{xx} - [\rho_t]_1 D_x^1[p_f] - [\rho_t]_1 \frac{[\eta_f]_1}{[k]_1} \bar{D}_\chi [q_f^D]\right), \tag{E14}$$

$$D_t^2[v_x^s] = \frac{1}{[\Theta]_1}\left([\rho_a]_1 \nabla \cdot \bar{\sigma}_{xx} + [\rho_f]_1 D_x^1[p_f] + [\rho_f]_1 \frac{[\eta_f]_1}{[k]_1} \bar{D}_\chi [q_f^D]\right). \tag{E15}$$

Appendix F: The GPU Architecture

GPUs feature a hierarchic structure. The basic computational unit is the Thread. Threads are organized in blocks of Threads that constitute the Grid. A GPU function (CUDA kernel) executes in as many concurrent instances as the total amount of Threads, that is, the Threads per Block times the amount of Blocks. We assign each data unit (grid cell) of our computational domain to a specific Thread; the identical numerical operation performed on each data unit (grid cell) will thus be executed simultaneously in the entire computational domain (Figure F1).

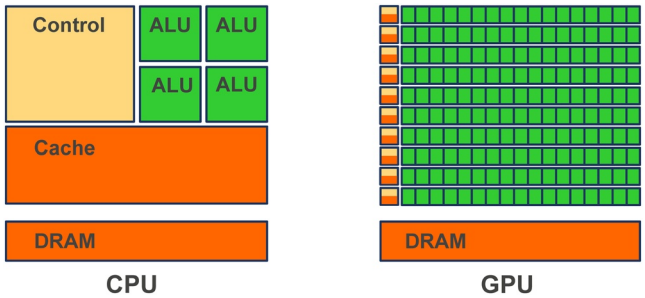

Figure F1. Schematic chip representation for both the central processing unit (CPU) and graphical processing unit (GPU) architectures. The GPU architecture consist of thousands of arithmetic and logical units (ALU). On the CPU, most of the on-chip space is devoted to controlling units and cache memory, while the number of ALUs is significantly reduced.

Data Availability Statement

No data were used in producing this manuscript. The routines to reproduce the main presented results are available for download from Bitbucket at https://bitbucket.org/yalkhimenkov/fastbiot_gpu3d_v1.0 (last access: February 8, 2021). The routines archive (v1.0) (Alkhimenkov et al., 2021) is available from a permanent DOI repository (Zenodo) at http://doi.org/10.5281/zenodo.4519367 (last access: February 8, 2021).

Acknowledgments
This research is funded by the Swiss National Science Foundation, project number 172691. Y. Alkhimenkov, L. Khakimova, and Y. Podladchikov gratefully acknowledge support from the Ministry of Science and Higher Education of the Russian Federation (project No. 075-15-2019-1890). Y. Alkhimenkov thanks Y. Masson for fruitful discussions regarding the stability of the discretized Biot's equations. L. Räss thanks Samuel Omlin for fruitful discussions regarding the multi-GPU implementation. The authors thank Philippe Logean for technical support and the Swiss Geocomputing Center for providing computational resources.

References

Alkhimenkov, Y., Khakimova, L., & Podladchikov, Y. (2020). Stability of discrete schemes of Biot's poroelastic equations. *Geophysical Journal International*, *225*, 354–377. https://doi.org/10.1093/gji/ggaa584

Alkhimenkov, Y., Räss, L., Khakimova, L., Quintal, B., & Podladchikov, Y. (2021). *Fastbiot_gpu3d*. Zenodo. https://doi.org/10.5281/zenodo.4519367

Biot (1965). *Mechanics of incremental deformations*. John Wiley & Sons. Retrieved from https://hal.archives-ouvertes.fr/hal-01352219

Biot, & Willis, D. (1957). The elastic coefficients of the theory of consolidation. *Journal of Applied Mechanics*, *15*, 594–601. https://doi.org/10.1090/qam/87469

Biot, M. A. (1941). General theory of three-dimensional consolidation. *Journal of Applied Physics*, *12*(2), 155–164. https://doi.org/10.1063/1.1712886

Biot, M. A. (1956a). Theory of propagation of elastic waves in a fluid-saturated porous solid. I. Low-frequency range. *Journal of the Acoustical Society of America*, *28*(2), 168–178. https://doi.org/10.1121/1.1908239

Biot, M. A. (1956b). Theory of propagation of elastic waves in a fluid-saturated porous solid. II. Higher frequency range. *Journal of the acoustical Society of America*, *28*(2), 179–191. https://doi.org/10.1121/1.1908241

Biot, M. A. (1962a). Generalized theory of acoustic propagation in porous dissipative media. *Journal of the Acoustical Society of America*, *34*(9A), 1254–1264. https://doi.org/10.1121/1.1918315

Biot, M. A. (1962b). Mechanics of deformation and acoustic propagation in porous media. *Journal of Applied Physics*, *33*(4), 1482–1498. https://doi.org/10.1063/1.1728759

Blanc, E., Chiavassa, G., & Lombard, B. (2013). A time-domain numerical modeling of two-dimensional wave propagation in porous media with frequency-dependent dynamic permeability. *Journal of the Acoustical Society of America*, *134*(6), 4610–4623. https://doi.org/10.1121/1.4824832

Bourbié, T., Coussy, O., Zinszner, B., & Junger, M. C. (1987). *Acoustics of porous media*. Gulf Publishing Company.

Carcione, J. M. (2014). *Wave fields in real media: Wave propagation in anisotropic, anelastic, porous and electromagnetic media*. Elsevier.

Carcione, J. M., Morency, C., & Santos, J. E. (2010). Computational poroelasticity - A review. *Geophysics*, *75*(5), 75A229–75A243. https://doi.org/10.1190/1.3474602

Carcione, J. M., & Quiroga-Goode, G. (1995). Some aspects of the physics and numerical modeling of biot compressional waves. *Journal of Computational Acoustics*, *03*(04), 261–280. https://doi.org/10.1142/s0218396x95000136

Caspari, E., Novikov, M., Lisitsa, V., Barbosa, N. D., Quintal, B., Rubino, J. G., & Holliger, K. (2019). Attenuation mechanisms in fractured fluid-saturated porous rocks: A numerical modelling study. *Geophysical Prospecting*, *67*(4), 935–955. https://doi.org/10.1111/1365-2478.12667

Cheng, A. H.-D. (2016). *Poroelasticity* (Vol. 877). Springer.

Chiavassa, G., & Lombard, B. (2011). Time domain numerical modeling of wave propagation in 2d heterogeneous porous media. *Journal of Computational Physics*, *230*(13), 5288–5309. https://doi.org/10.1016/j.jcp.2011.03.030

Chiavassa, G., Lombard, B., & Piraux, J. (2010). Numerical modeling of 1d transient poroelastic waves in the low-frequency range. *Journal of Computational and Applied Mathematics*, *234*(6), 1757–1765. https://doi.org/10.1016/j.cam.2009.08.025

CUDA C. (2020). *Programming guide*.

Dai, N., Vafidis, A., & Kanasewich, E. R. (1995). Wave propagation in heterogeneous, porous media: A velocity-stress, finite-difference method. *Geophysics*, *60*(2), 327–340. https://doi.org/10.1190/1.1443769

Davydycheva, S., Druskin, V., & Habashy, T. (2003). An efficient finite-difference scheme for electromagnetic logging in 3D anisotropic inhomogeneous media. *Geophysics*, *68*(5), 1525–1536. https://doi.org/10.1190/1.1620626

de la Puente, J., Dumbser, M., Käser, M., & Igel, H. (2008). Discontinuous galerkin methods for wave propagation in poroelastic media. *Geophysics*, *73*(5), T77–T97. https://doi.org/10.1190/1.2965027

Dormy, E., & Tarantola, A. (1995). Numerical simulation of elastic wave propagation using a finite volume method. *Journal of Geophysical Research*, *100*(B2), 2123–2133. https://doi.org/10.1029/94jb02648

Dupuy, B., De Barros, L., Garambois, S., & Virieux, J. (2011). Wave propagation in heterogeneous porous media formulated in the frequency-space domain using a discontinuous galerkin method. *Geophysics*, *76*(4), N13–N28. https://doi.org/10.1190/1.3581361

Duretz, T., Räss, L., Podladchikov, Y., & Schmalholz, S. (2019). Resolving thermomechanical coupling in two and three dimensions: Spontaneous strain localization owing to shear heating. *Geophysical Journal International*, *216*(1), 365–379. https://doi.org/10.1093/gji/ggy434

Dvorkin, J., Mavko, G., & Nur, A. (1995). Squirt flow in fully saturated rocks. *Geophysics*, *60*(1), 97–107. https://doi.org/10.1190/1.1443767

Frenkel, J. (1944). On the theory of seismic and seismoelectric phenomena in a moist soil. *Journal of Physics*, *III*(4), 230–241. https://doi.org/10.1061/(ASCE)0733-9399(2005)131:9(879)

Gregor, D., Moczo, P., Kristek, J., Mesgouez, A., Lefeuve-Mesgouez, G., & Kristekova, M. (2021). Subcell-resolution finite-difference modeling of seismic waves in biot and jkd poroelastic media. *Geophysical Journal International*, *224*(2), 760–794. https://doi.org/10.1093/gji/ggaa454

Harlow, F. H., & Welch, J. E. (1965). Numerical calculation of time-dependent viscous incompressible flow of fluid with free surface. *Physics of Fluids*, *8*(12), 2182–2189. https://doi.org/10.1063/1.1761178

Hunziker, J., Favino, M., Caspari, E., Quintal, B., Rubino, J. G., Krause, R., & Holliger, K. (2018). Seismic attenuation and stiffness modulus dispersion in porous rocks containing stochastic fracture networks. *Journal of Geophysical Research: Solid Earth*, *123*(1), 125–143. https://doi.org/10.1002/2017jb014566

Jou, D., Casas-Vázquez, J., & Lebon, G. (2001). *Extended irreversible thermodynamics* (3rd ed., pp. 462). Berlin: Springer.

Komatitsch, D., Erlebacher, G., Göddeke, D., & Michéa, D. (2010). High-order finite-element seismic wave propagation modeling with mpi on a large gpu cluster. *Journal of Computational Physics*, *229*(20), 7692–7714. https://doi.org/10.1016/j.jcp.2010.06.024

Lebedev, V. I. (1964). Difference analogs of orthogonal decompositions, basic differential operators and some boundary problems of mathematical physics. i. *USSR Computational Mathematics and Mathematical Physics*, *4*(3), 69–92. https://doi.org/10.1016/0041-5553(64)90240-x

Lemoine, G. I. (2016). Three-dimensional mapped-grid finite volume modeling of poroelastic-fluid wave propagation. *SIAM Journal on Scientific Computing*, *38*(5), B808–B836. https://doi.org/10.1137/130934866

Lemoine, G. I., Ou, M. Y., & LeVeque, R. J. (2013). High-resolution finite volume modeling of wave propagation in orthotropic poroelastic media. *SIAM Journal on Scientific Computing*, *35*(1), B176–B206. https://doi.org/10.1137/120878720

Levander, A. R. (1988). Fourth-order finite-difference P-SV seismograms. *Geophysics*, *53*(11), 1425–1436. https://doi.org/10.1190/1.1442422

LeVeque, R. J. (1992). *Numerical Methods for Conservation Laws* (Vol. 132). Springer. https://doi.org/10.1007/978-3-0348-5116-9

Lisitsa, V., & Vishnevskiy, D. (2010). Lebedev scheme for the numerical simulation of wave propagation in 3D anisotropic elasticity. *Geophysical Prospecting*, *58*(4), 619–635. https://doi.org/10.1111/j.1365-2478.2009.00862.x

Makhnenko, R. Y., & Podladchikov, Y. Y. (2018). Experimental poroviscoelasticity of common sedimentary rocks. *Journal of Geophysical Research: Solid Earth*, *123*(9), 7586–7603. https://doi.org/10.1029/2018jb015685

Masson, Y. J., & Pride, S. R. (2007). Poroelastic finite difference modeling of seismic attenuation and dispersion due to mesoscopic-scale heterogeneity. *Journal of Geophysical Research*, *112*(B3), B3204. https://doi.org/10.1029/2006jb004592

Masson, Y. J., Pride, S. R., & Nihei, K. (2006). Finite difference modeling of biot's poroelastic equations at seismic frequencies. *Journal of Geophysical Research*, *111*(B10), B10305. https://doi.org/10.1029/2006jb004366

Mavko, G., & Nur, A. (1975). Melt squirt in the asthenosphere. *Journal of Geophysical Research*, *80*(11), 1444–1448. https://doi.org/10.1029/jb080i011p01444

McKee, S., Tomé, M. F., Ferreira, V. G., Cuminato, J. A., Castelo, A., Sousa, F. S., & Mangiavacchi, N. (2008). The mac method. *Computers & Fluids*, *37*(8), 907–930. https://doi.org/10.1016/j.compfluid.2007.10.006

Mehra, R., Raghuvanshi, N., Savioja, L., Lin, M. C., & Manocha, D. (2012). An efficient gpu-based time domain solver for the acoustic wave equation. *Applied Acoustics*, *73*(2), 83–94. https://doi.org/10.1016/j.apacoust.2011.05.012

Michéa, D., & Komatitsch, D. (2010). Accelerating a three-dimensional finite-difference wave propagation code using gpu graphics cards. *Geophysical Journal International*, *182*(1), 389–402. https://doi.org/10.1111/j.1365-246X.2010.04616.x

Moczo, P., Gregor, D., Kristek, J., & de la Puente, J. (2019). A discrete representation of material heterogeneity for the finite-difference modeling of seismic wave propagation in a poroelastic medium. *Geophysical Journal International*, *216*(2), 1072–1099. https://doi.org/10.1093/gji/ggy412

Moczo, P., Robertsson, J. O. A., & Eisner, L. (2007). The finite-difference time-domain method for modeling of seismic wave propagation. *Advances in Geophysics*, *48*, 421–516. https://doi.org/10.1016/s0065-2687(06)48008-0

Morency, C., & Tromp, J. (2008). Spectral-element simulations of wave propagation in porous media. *Geophysical Journal International*, *175*(1), 301–345. https://doi.org/10.1111/j.1365-246x.2008.03907.x

Müller, T. M., Gurevich, B., & Lebedev, M. (2010). Seismic wave attenuation and dispersion resulting from wave-induced flow in porous rocks - A review. *Geophysics*, *75*(5), 75A147–75A164. https://doi.org/10.1190/1.3463417

Omlin, S. (2016). *Development of massively parallel near peak performance solvers for three-dimensional geodynamic modeling (Unpublished doctoral dissertation)*. Université de Lausanne, Faculté des géosciences et de l'environnement.

Omlin, S., Räss, L., Kwasniewski, G., Malvoisin, B., Omlin, S., & Podladchikov, Y. (2020). *Solving nonlinear multi-physics on gpu supercomputers with julia*. GTC Silicon Valley - 2019. 2019b https://developer.nvidia.com/gtc/2019/video/S9368

Özdenvar, T., & McMechan, G. A. (1997). Algorithms for staggered-grid computations for poroelastic, elastic, acoustic, and scalar wave equations. *Geophysical Prospecting*, *45*(3), 403–420. https://doi.org/10.1046/j.1365-2478.1997.390275.x

Pride, S. R., Berryman, J. G., & Harris, J. M. (2004). Seismic attenuation due to wave-induced flow. *Journal of Geophysical Research: Solid Earth*, *109*(B1). no. B1.B01201. https://doi.org/10.1029/2003jb002639

Pride, S. R., & Garambois, S. (2005). Electroseismic wave theory of frenkel and more recent developments. *Journal of Engineering Mechanics*, *131*(9), 898–907. https://doi.org/10.1061/(asce)0733-9399(2005)131:9(898)

Quintal, B., Steeb, H., Frehner, M., & Schmalholz, S. M. (2011). Quasi-static finite element modeling of seismic attenuation and dispersion due to wave-induced fluid flow in poroelastic media. *Journal of Geophysical Research*, *116*(B1), B01201. https://doi.org/10.1029/2010jb007475

Räss, L., Duretz, T., & Podladchikov, Y. Y. (2019). Resolving hydromechanical coupling in two and three dimensions: spontaneous channeling of porous fluids owing to decompaction weakening. *Geophysical Journal International*, *218*(3), 1591–1616. https://doi.org/10.1093/gji/ggz239

Räss, L., Duretz, T., Podladchikov, Y. Y., & Schmalholz, S. M. (2017). M2Di: Concise and efficient MATLAB 2-D stokes solvers using the finite difference method. *Geochemistry Geophysics Geosystem*, *18*(2), 755–768. https://doi.org/10.1002/2016gc006727

Räss, L., Licul, A., Herman, F., Podladchikov, Y. Y., & Suckale, J. (2020). Modeling thermomechanical ice deformation using an implicit pseudo-transient method (FastICE v1.0) based on graphical processing units (GPUs). *Geoscientific Model Development*, *13*(3), 955–976. https://doi.org/10.5194/gmd-13-955-2020

Räss, L., Omlin, S., & Podladchikov, Y. (2019). *Resolving spontaneous nonlinear multi-physics flow localization in 3-D: Tackling hardware limit*. GTC Silicon Valley - 2019, 2019b. https://developer.nvidia.com/gtc/2019/video/S9368

Rubino, J. G., Ravazzoli, C. L., & Santos, J. E. (2009). Equivalent viscoelastic solids for heterogeneous fluid-saturated porous rocks. *Geophysics*, *74*(1), N1–N13. https://doi.org/10.1190/1.3008544

Rubio, F., Hanzich, M., Farrés, A., De La Puente, J., & María Cela, J. (2014). Finite-difference staggered grids in gpus for anisotropic elastic wave propagation simulation. *Computers & Geosciences*, *70*, 181–189. https://doi.org/10.1016/j.cageo.2014.06.003

Saenger, E. H., Gold, N., & Shapiro, S. A. (2000). Modeling the propagation of elastic waves using a modified finite-difference grid. *Wave Motion*, *31*(1), 77–92. https://doi.org/10.1016/s0165-2125(99)00023-2

Shukla, K., Chan, J., Maarten, V., & Jaiswal, P. (2020). A weight-adjusted discontinuous galerkin method for the poroelastic wave equation: penalty fluxes and micro-heterogeneities. *Journal of Computational Physics*, *403*, 109061. https://doi.org/10.1016/j.jcp.2019.109061

Shukla, K., Hesthaven, J. S., Carcione, J. M., Ye, R., de la Puente, J., & Jaiswal, P. (2019). A nodal discontinuous galerkin finite element method for the poroelastic wave equation. *Comput Geosci*, *23*(3), 595–615. https://doi.org/10.1007/s10596-019-9809-1

Virieux, J. (1986). P-SV wave propagation in heterogeneous media: Velocity-stress finite-difference method. *Geophysics*, *51*(4), 889–901. https://doi.org/10.1190/1.1442147

Virieux, J., & Madariaga, R. (1982). Dynamic faulting studied by a finite difference method. *Bulletin of the Seismological Society of America*, *72*(2), 345–369.

Wang, H. F. (2000). *Theory of linear poroelasticity with applications to geomechanics and hydrogeology*. Princeton University Press.

Ward, N. D., Lähivaara, T., & Eveson, S. (2017). A discontinuous galerkin method for poroelastic wave propagation: The two-dimensional case. *Journal of Computational Physics*, *350*, 690–727. https://doi.org/10.1016/j.jcp.2017.08.070

Weiss, R. M., & Shragge, J. (2013). Solving 3d anisotropic elastic wave equations on parallel gpu devices. *Geophysics*, *78*(2), F7–F15. https://doi.org/10.1190/geo2012-0063.1

Wenzlau, F., & Müller, T. M. (2009). Finite-difference modeling of wave propagation and diffusion in poroelastic media. *Geophysics*, *74*(4), T55–T66. https://doi.org/10.1190/1.3122928

White, J. E., Mihailova, N., & Lyakhovitsky, F. (1975). Low-frequency seismic waves in fluid-saturated layered rocks. *Journal of the Acoustical Society of America*, *57*(S1), S30. https://doi.org/10.1121/1.1995164

Yarushina, V. M., & Podladchikov, Y. Y. (2015). (De)compaction of porous viscoelastoplastic media: Model formulation. *Journal of Geophysical Research: Solid Earth*, *120*(6), 4146–4170. https://doi.org/10.1002/2014jb011258

Zeng, Y. Q., He, J. Q., & Liu, Q. H. (2001). The application of the perfectly matched layer in numerical modeling of wave propagation in poroelastic media. *Geophysics*, *66*(4), 1258–1266. https://doi.org/10.1190/1.1487073

Zhan, Q., Zhuang, M., Fang, Y., Hu, Y., Mao, Y., Huang, W.-F., et al., (2019). Full-anisotropic poroelastic wave modeling: A discontinuous galerkin algorithm with a generalized wave impedance. *Computer Methods in Applied Mechanics and Engineering*, *346*, 288–311. https://doi.org/10.1016/j.cma.2018.12.003

Zhu, X., & McMechan, G. A. (1991). Numerical simulation of seismic responses of poroelastic reservoirs using biot theory. *Geophysics*, *56*(3), 328–339. https://doi.org/10.1190/1.1443047

Zimmerman, R. W. (1990). *Compressibility of sandstones*. Elsevier.

Zimmerman, R. W. (2000). Coupling in poroelasticity and thermoelasticity. *International Journal of Rock Mechanics and Mining Sciences*, *37*(1–2), 79–87. https://doi.org/10.1016/s1365-1609(99)00094-5